ACCSCIENCE PUBLISHING

International Journal of Bioprinting

RESEARCH ARTICLE

Three-dimensional-printed bionic dual crosslinked drug-loaded hydrogel composite scaffolds for large bone defect repair

Xulin Hu[1,2†*], Zhen Zhang[3†], Lijin Ning[4†], Yixuan Lan[1], Wang Gong[1], Jiayu Liu[1], Shuhao Yang[5], Haoming Wu[1], Weiming Zhao[1], Jian He[6], Kainan Li[1*], and Weizong Weng[7,8*]

[1] Department of Orthopedics, Clinical Medical College and Affiliated Hospital of Chengdu University, Chengdu University, Chengdu, Sichuan, China

[2] Department of Biotherapy, Cancer Center and State Key Laboratory of Biotherapy, West China Hospital, Sichuan University, Chengdu, Sichuan, China

[3] Department of Chemistry, Chengdu Institute of Organic Chemistry, Chinese Academy of Sciences, Chengdu, Sichuan, China

[4] Department of Dentistry, School of Jinzhou Medical University, Jinzhou Medical University, Jinzhou, Liaoning, China.

[5] Department of Orthopedics, The First Affiliated Hospital of Chongqing Medical University, Chongqing, China

[6] Department of Basic Medicine, Faculty of Medicine, Henan University of Science and Technology, Luoyang, Henan, China

[7] Department of Orthopaedics, Chenggong Hospital, Xiamen University, Xiamen, Fujian, China

[8] Department of Orthopedics, Institute of Translational Medicine, Shanghai University, Shanghai, China

[†]These authors contributed equally to this work.

***Corresponding authors:**
Xulin Hu
(huxulin1993@163.com)

Kainan Li
(likainan1961cdfy@126.com)

Weizong Weng
(drwengweizong@163.com)

Citation: Hu X, Zhang Z, Ning L, *et al.* Three-dimensional-printed bionic dual crosslinked drug-loaded hydrogel composite scaffolds for large bone defect repair. *Int J Bioprint.* 2026;12(1):348-370. doi: 10.36922/IJB025380391

Received: September 21, 2025
1st revised: October 20, 2025
2nd revised: November 5, 2025
Accepted: November 12, 2025
Published online: November 12, 2025

Abstract

The structure, composition, and function of natural bone have long been the focus of bone tissue engineering. However, existing organic–inorganic three-dimensional (3D) printing systems are limited by the stability of hydrogels and the content of inorganic salts, hindering the fabrication of robust 3D scaffolds. In this study, we developed a hydrogel–inorganic particle bioink and implemented a multi-step crosslinking strategy. The organic phase, composed of sodium alginate, gelatin, and chitosan, was combined with β-tricalcium phosphate and crosslinked via ionic pre-crosslinking followed by a Schiff base reaction to form a dual-crosslinked network. The resulting scaffolds exhibited excellent mechanical properties and biomimetic microarchitecture while maintaining shape stability under physiological conditions. Furthermore, the tunable swelling behavior of the hydrogel enabled efficient loading and controlled release of the small molecule epigallocatechin gallate. This composite scaffold demonstrated adjustable swelling, controllable degradation, and significantly enhanced cellular compatibility, providing a novel, efficient, and scalable strategy for repairing complex bone defects and offering new insights for the design and application of 3D-printed bone scaffolds.

***Keywords*:** β-tricalcium phosphate; Bionic tissue structure; Hydrogel base; Three-dimensional printing

1. Introduction

Bone loss, instigated by severe trauma and infectious diseases, is a pressing concern affecting millions globally. Recent studies indicate that approximately three million cases annually are related to significant bone loss due to these causes.[1] Depending on the extent of the damage, bone loss can be categorized into two types: minor bone loss (less than 2 cm of bone length affected) and major bone loss (more than 2 cm of bone length affected).[2–5] When comparing the two, bones with a minor loss have a 70% self-healing rate, whereas those with major bone loss exhibit a self-healing capability of only 30%. Current traditional treatments for major bone loss, such as bone grafting, have only a 50% success rate, highlighting the difficulty in addressing substantial clinical needs. In this regard, researchers have proposed the employment of artificial bones to solve the current clinical problem of large bone loss.[6,7]

Artificial bone is a synthetic or biological material engineered to emulate the structure and function of natural bone, intended for the treatment of fractures or the repair of bone defects.[8] Bone is a complex structural tissue primarily composed of cortical bone and cancellous bone.[9–11] Cortical bone, also known as compact bone, predominantly forms the external layer of bones, providing them with strength and support.[12] In contrast, cancellous bone, often referred to as trabecular or spongy bone, is primarily found within the interior regions of bones, such as the ends of long bones and in flat bones. Its unique porous structure, characterized by an intricate network of trabeculae interspersed with marrow-filled spaces, plays a pivotal role in the biological processes of bone, especially in bone repair and remodeling. The extensive surface area of cancellous bone, coupled with the marrow it houses, offers a rich reservoir of cells and growth factors vital for bone regeneration. Therefore, cancellous bone is often considered the primary component of repair in research.[13–16] During the bone healing process, multiple types of cells are involved, including osteoblasts, osteoclasts, osteocytes, and chondrocytes. These cells are primarily responsible for forming bone and cartilage in bone tissue. Osteoclasts are mainly responsible for the absorption of bone cells.[17] The average bone balance is achieved by regulating the relationship between osteoblasts and osteoclasts. The repair process of bone injury requires the coordination of multiple histological processes and different biochemical stages. It can be divided into three stages: the inflammatory stage, the stage of granulation tissue formation, and the remodeling stage of the tissue.[18,19] Studies have shown that bionic tissue structures can imitate the micro- and macrostructures of bone tissue, provide cells with a growth environment similar to their natural environment,[20] and offer cells similar physical and chemical signals, thereby promoting their natural proliferation and growth (Figure 1).[21–23]

In the field of biomaterials science, hydrogels are engineered to possess a three-dimensional, porous

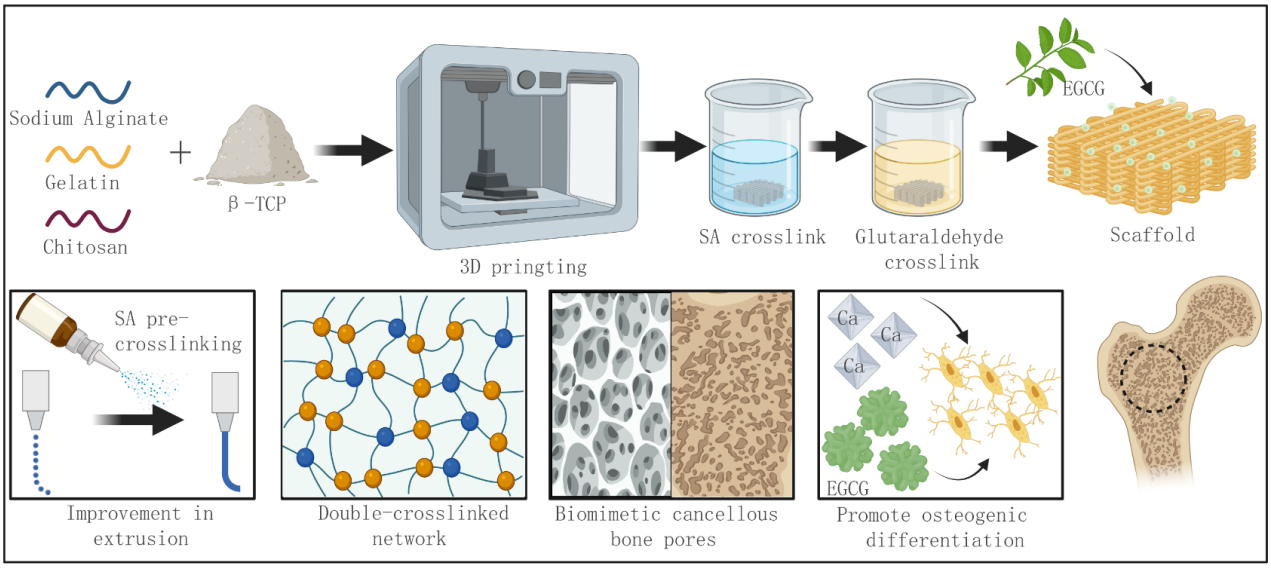

Figure 1. Schematic illustration of a biomimetically multilevel three-dimensional (3D) printing scaffold for repairing large bone defects. Different materials are physically blended to form a bioink suitable for 3D printing. A dual-crosslinking strategy endows the scaffold with stable, comprehensive properties and a biomimetic tissue structure, and the scaffold is loaded with drugs to promote the repair of large bone defects. Abbreviations: β-TCP, β-tricalcium phosphate; EGCG, epigallocatechin gallate; H&E, hematoxylin & eosin; CT, computed tomography.

structure that closely mimics the nanofibrous architecture of native extracellular matrices (ECM). This biomimicry is achieved through the careful design of hydrogel networks to replicate ECM components such as collagen and glycosaminoglycans, facilitating cellular attachment, proliferation, and differentiation.[24–25] While hydrogels with such intrinsically biomimetic structures have found applications in wound dressings, ophthalmic devices, and other biomedically relevant areas, their deployment in bone tissue engineering remains limited.[26–28] One primary limitation is their poor stability, especially in the dynamic and multifaceted environment of physiological fluids. Additionally, the inherent mechanical properties of hydrogels often fall short of the rigorous biomechanical demands expected of bone scaffolds. These challenges necessitate further research and innovation to harness the potential of hydrogels in bone tissue regeneration.[26,29] In recent research, Nie et al. compounded hydrogels with inorganic ceramic materials to prepare scaffolds through 3D printing technology and achieved a bionic tissue structure inside the scaffold. However, after testing the mechanical properties of the scaffold, they found that the compressive modulus of the scaffold was significantly lower.[30] According to our analysis, the lower the compressive modulus is, the larger the pore structure of the three-dimensional network formed. This is due to the polymer formed by a single cross-linked hydrogel. Adhesion between the polymer networks will occur during the freeze-drying process (when water molecules are removed, the interactions between polymer chains may become more closely connected, such as van der Waals forces and hydrogen bonds). This will cause adhesion between polymer chains.). In this regard, we found that as early as 2005, some researchers proposed a double network structure.[31] The so-called double network refers to a polymer network formed by cross-linking two different polymers. When freeze drying, due to its unique combination during the process, the dual network structure can better cope with the stress generated, thereby reducing the damage of ice crystals to the network structure, ensuring a relatively stable network structure and enabling the scaffold to have a more penetrating and tight interpenetrating network connection. It can improve the compression modulus of the stent and maintain the application accuracy of the scaffold.[32–34]

This study aims to use 3D printing technology to prepare a hydrogel-based composite scaffold with a bionic tissue structure and stable mechanical properties (Figure 1). Sodium alginate, a linear anionic polysaccharide with excellent cross-linking properties, is selected as the base, and calcium ions are selected for cross-linking,[35–37] together with the crosslinking molding of gelatin, a double crosslinked double network system is formed to enhance the stability of the hydrogel and. In the dual-crosslinking system, chemical crosslinking provides the composite system with a certain degree of strength and mechanical stability, while physical crosslinking not only maintains the drug-loading capacity of the hydrogel components but also contributes to energy dissipation. Considering the reduction of cell-binding sites in gelatin after crosslinking, chitosan with strong cell adhesion was introduced.[38–41] At the same time, To enhance the osteogenic differentiation capability of the hydrogel system and maintain the shape stability of the hydrogel-based scaffold during the degradation process, add a certain proportion of β-tricalcium phosphate to the hydrogel, which can release calcium ions during the degradation process.[42] After compounding with hydrogel, prepare bioink and use an extrusion Bio-3D printer with precross-linking Strategies for printing composite scaffolds. After analyzing a series of properties of the composite scaffold, we found that the prepared composite scaffold has a bionic tissue structure and can effectively promote cell proliferation and differentiation. It also has certain mechanical properties to meet the mechanical properties of the implanted scaffold in the early stage of bone healing requirements. At the same time, the hydrogel component was used to realize the payload of the drug EGCG. Animal experiment results show that the prepared scaffold has excellent in vivo osteogenic properties.

2. Materials and methodology

2.1. Materials

Sodium alginate (SA; 216.126 kDa), chitosan (degree of deacetylation ≥ 95%), anhydrous calcium chloride, and gelatin (Gel) were obtained from Shanghai Aladdin Bio (China), while β-tricalcium phosphate (β-TCP) was purchased from Kunshan Chinese Technology New Materials (China). Epigallocatechin gallate (EGCG) was provided by the Tea Research Institute of the Chinese Academy of Agricultural Sciences (China). Glutaraldehyde was provided by the West China Hospital of Sichuan University (China).

2.2. Preparation of bioink

In the initial phase of the experiment, without altering the chitosan content, we screened various hydrogel compositions (comprising SA and Gel in different ratios). Our evaluation criteria were based on simple mechanical properties and porosity (Figure S1), as well as the subsequent printability of the biological ink. Ultimately, we selected a hydrogel composition consisting of 3% SA, 2% chitosan, and 10% Gel. The preparation process of the bioink can be divided into two stages. For the preparation of the hydrogel precursor solution, SA powder was weighed

Table 1. Distribution ratio of each group of bioink

Group	Sodium alginate (w/v%)	Chitosan (w/v%)	Gelatin (w/v%)	β-tricalcium phosphate (w/v%)
SCG	3%	2%	10%	0
SCG-30%	3%	2%	10%	30%
SCG-40%	3%	2%	10%	40%
SCG-50%	3%	2%	10%	50%

according to the ratios shown in Table 1. The measured amount was then placed in a beaker, and deionized water was added to it. The mixture was stirred at 300 rpm using a magnetic stirrer for 2 h to ensure complete dissolution of SA, yielding a 3% SA solution. Subsequently, a measured quantity of chitosan powder was added directly to the SA solution, and the mixture was stirred at 200 rpm for 3 h to achieve uniform dispersion of chitosan in the SA precursor, resulting in a 3% SA + 2% chitosan hydrogel precursor solution.

Next, the Gel was weighed according to the proportions shown in Table 1 and stirred mechanically to disperse the Gel evenly. The sealed beaker was placed in a water bath at 60°C until the Gel completely dissolved. During this process, periodic replenishment of water was performed to maintain constant concentrations of the bioink components. After complete Gel dissolution, the precursor solution was transferred to a 60°C oven and subjected to intermittent heating (30 min each time) until most of the bubbles were removed. At this point, the preparation of the hydrogel components was concluded. The formulated hydrogel precursor solution was stored at 4°C for subsequent use.

After preparing the hydrogel precursor solution, different proportions of β-TCP were added to create a bioink. The specific procedure involved initial grinding and sieving of the β-TCP powder to ensure printability. The β-TCP powder was placed in a mortar and mechanically ground for 1 h, followed by sieving through a 200-mesh sieve to control the particle size of β-TCP to less than 80 μm. Subsequently, the previously prepared hydrogel precursor solution was dissolved in a water bath at 60°C. A specific volume of the hydrogel precursor solution was then extracted according to preestablished ratios and mixed with the sieved β-TCP. This completed the preparation of the bioink, ensuring its printability for subsequent applications. The pure hydrogel component was designated SCG, while the addition of various β-TCP components was named SCG-30%, SCG-40%, and SCG-50%.

2.3. Selection and characterization of crosslinking strategies for bioink

The specific operational steps were as follows: a specific amount of anhydrous calcium chloride was weighed and dissolved in deionized water to prepare a 0.6% (w/v) calcium ion solution. To ensure a good dissolution of chitosan, a specific amount of glacial acetic acid was added dropwise to the prepared calcium ion solution, adjusting the solution to a weakly acidic condition with a pH of 4.8. The scaffold was immersed in an acidic calcium ion solution for 3 h to ensure complete crosslinking of SA in the composition. The crosslinking of Gel is crucial for maintaining the stability of the hydrogel structure. Previous studies have shown that the degree of Gel crosslinking affects both cell compatibility and structural stability. A commonly used Gel crosslinking agent is glutaraldehyde, and a concentration of 0.6% (v/v) glutaraldehyde was chosen. The crosslinking of Gel in the hydrogel was carried out at 50°C for 3 h to achieve optimal crosslinking effects. This choice aimed to utilize the lowest concentration of glutaraldehyde to achieve the best crosslinking results. After crosslinking, the hydrogel was washed thoroughly at least three times to remove residual crosslinking agents from the hydrogel surface. Through this two-step crosslinking process, a dual-crosslinked interpenetrating network system consisting of both physical and chemical crosslinks was established, significantly enhancing the stability and mechanical properties of the hydrogel system.

2.4. Analysis of gelation ability and relevant physicochemical characterization of bioink

The calcium ion-crosslinked hydrogel component used in this study was SA. Studies have shown that higher calcium ion concentrations form a dense surface film on the hydrogel, reducing calcium ion entry and thus crosslinking. Choosing a lower calcium ion concentration will result in better crosslinking. In this study, a calcium ion concentration of 0.6% was used. Since the concentration was low, we first evaluated the gel-forming effect of the bioink to determine the crosslinking effect of calcium ions on SA. The gelation effect of calcium ion crosslinking on the hydrogel was determined using an inclined and inverted method. Specifically, the prepared hydrogel precursor solution was dissolved in a 60°C water bath. After dissolution, 2.5 mL of the hydrogel precursor solution was extracted and placed in a bottle. Subsequently, 1 mL of a preprepared 0.6% w/v acidic calcium chloride solution was added. To exclude the influence of the temperature-sensitive characteristics of Gel, the bottle was consistently

heated in a 37°C water bath. Five time points (1 min, 5 min, 10 min, 30 min, and 60 min) were selected, and the calcium ions were poured out of the bottle at each time point.

2.4.1. Fourier transform infrared spectra analysis

To analyze the changes in groups between the components of the scaffold after preparation and crosslinking, a Fourier transform infrared (EQUINX55, Brücher Crop, Germany) analysis was conducted. Data were scanned and collected across the spectral range of 500–4000/cm. The obtained spectral data underwent in-depth analysis and graphical representation using the ORIGIN software (OriginPro 2023).

2.4.2. Hydrophilicity evaluation

Hydrophilicity was assessed using a contact angle measurement instrument (CA200, Ysenmed, China). Composite hydrogel films with varying components were prepared and polished to achieve uniform surfaces. The films were subjected to deionized water droplets dispensed at a rate of 5 μL/s. After a 10-s equilibrium, images were captured and analyzed for contact angle using dedicated software (ImageJ 1.53). This process was repeated three times for each composite hydrogel, ensuring reliability in evaluating the hydrophilic characteristics of the films in contact with water.

2.4.3. Equilibrium swelling test

To assess the equilibrium swelling properties of the hydrogel, the following steps were employed. The bioink was placed within a cylindrical mold (10 × 5 mm) to form cylindrical hydrogel samples. After crosslinking and freeze-drying, the dried composite hydrogel was obtained. Three samples per group were weighed to determine the dry weight (*Wd*). These samples were then immersed in phosphate-buffered saline at 37°C. At various time intervals, the scaffolds were removed, excess surface water was gently absorbed using absorbent paper, and the samples were reweighed (*Ww*) at each time point. The swelling ratio (*SR*) was calculated using **Equation (1)**:

$$SR = (Ww - Wd)/Wd \quad (1)$$

This process was repeated for each time point, providing insights into the hydrogel's capacity to absorb water over time.

2.5. Scaffold fabrication and characterization

2.5.1. Pre-crosslinking strategy

Since we chose a higher proportion of hydrogel to ensure the formation of a bionic structure inside the hydrogel, it is difficult to guarantee the molding accuracy of the scaffold. To ensure improved layer-to-layer structural integrity, a pre-crosslinking approach was employed. The specific steps for pre-crosslinking were as follows. The prepared bioink was placed in a constant-temperature water bath at 60°C until it was completely dissolved. Different ratios of calcium ion solution (0.2%, 0.4%, 0.6%, 0.8% w/v) were extracted using a syringe and then added to the bioink in a fixed proportion of 2:0.1 (v/v) of bioink to calcium ions. After the addition of the calcium ion solution, vigorous mechanical stirring was immediately initiated to continuously disrupt the gel state, thereby increasing the viscosity of the bioink. This process lasted for 5 min to ensure thorough mixing. Following mixing, scaffold printing commenced. Utilizing a biological three-dimensional (3D) printer (EFL-BP-6601, Yongqinquan Intelligent Equipment Co., Ltd., China) under the conditions of a selected 22-gauge printing needle (internal aperture 420 μm), printing speed of 10 mm/min, and pressure set at 100 kPa, scaffolds of different compositions were printed. The extrudability of the ink and the formation state of the printed scaffold were used as criteria for evaluating the pre-crosslinking concentration. The concentration of calcium ions used for scaffold pre-crosslinking was determined based on the ability of the ink to extrude into threads and the overall print quality of the scaffold.

2.5.2. Scaffold volume shrinkage analysis

Using a caliper, the dimensions were recorded, and the initial volume (*V*1) was calculated after crosslinking. After freeze-drying, measurements were taken, and the final volume (*V*2) was calculated. The volume shrinkage (P_s) was determined using **Equation (2)**:

$$Ps = \frac{V1 - V2}{V1} \times 100\% \quad (2)$$

This analysis informed the accuracy of the scaffold in scenarios involving bone defects.

2.5.3. Scaffold porosity analysis

The porosity of the composite scaffold was determined using Archimedes' principle of displacement. Initially, the volume of the freeze-dried scaffold, denoted as *V*1, was calculated using a Vernier caliper. Subsequently, 10 mL of anhydrous ethanol was placed in a test tube, with the liquid level marked at this point (ensuring it covered the scaffold). The scaffold was then placed into the test tube, sealed with sealing glue, and left undisturbed for 24 h. During this period, the test tube was gently tapped to allow any trapped air bubbles to escape. Upon complete infiltration of anhydrous ethanol into the interior of the scaffold, the height of the liquid level, *h*, was recorded. The inner diameter of the test tube, denoted as *d*, was measured using a Vernier caliper, and the volume change was

denoted as $V2$. The porosity (P) of the composite scaffold was calculated using **Equation (3)**:

$$P = \frac{V1 - V2}{V1} \times 100\% \quad V2 = \frac{\pi d^2}{4} \circ h \tag{3}$$

2.5.4. Microscopic characterization of the surface and cross-section of scaffolds

The freeze-dried scaffold was cryogenically fractured in liquid nitrogen. Subsequently, the microstructures of the surface and cross-sections of different scaffold components were observed under various magnifications using scanning electron microscopy (SEM; ZEISS Sigma 300, ZEISS, Germany). Additionally, the Nano Measurer software (version 1.2) was utilized to analyze the pore size distribution across the cross-sections.

2.5.5. Characterization of mechanical properties

The mechanical properties of different components of the freeze-dried scaffolds were analyzed using a universal testing machine (Instron 5967, China). The dimensions of the scaffolds were maintained at 10 × 10 × 5 mm, with three parallel samples for each group. Compression testing was conducted in accordance with the national standard GB/T 1041-2008. The testing parameters included a loading rate of 1 mm/min and a 5 kN load cell. The obtained stress–strain curves were used to calculate the compressive modulus, determined by the slope of the curve.

2.5.6. In vitro degradation performance evaluation of composite scaffolds

The Wd of the freeze-dried scaffold was denoted as $W1$. The scaffold was immersed in 15 mL of phosphate-buffered saline (pH 7.4) and continuously incubated at 37°C for 2, 4, and 8 weeks. At each time point, the scaffold was retrieved and thoroughly rinsed with deionized water to remove surface phosphate-buffered saline and mineralization. The weight of the scaffold measured after degradation was denoted as $W2$. Simultaneously, a pH meter was used to measure the pH of the degradation solution at various time points, documenting the changes in pH that occurred during the degradation process. The degradation rate (Pd) of the scaffold was evaluated using **Equation (4)**:

$$Pd = \frac{W1 - W2}{W1} \times 100\% \tag{4}$$

2.5.7. Characterization of in vitro mineralization capacity

Simultaneously, the degraded scaffold at the 8th week underwent compression testing using a universal testing machine after being rinsed and freeze-dried. The variation in compressive modulus between the degraded scaffold at the 8th week and the original composition was measured, and the percentage loss of compressive modulus was calculated.

2.5.8. In vitro mineralization

Under 37°C conditions, the scaffold was placed in a simulated body fluid, which facilitated the formation of hydroxyapatite on the material surface, predicting its *in vitro* bone bioactivity. The development of bone-like hydroxyapatite on the scaffold surface was observed using SEM at different time intervals, specifically at the 3rd, 7th, and 14th days. XRD (ARL Equinox 1000, Thermo Fisher Scientific, USA) was employed to analyze their crystalline structures.

2.5.9. Drug-loaded scaffold fabrication

Drug loading into the scaffold was achieved through the swelling principle of hydrogels. The loaded drug was EGCG, which possesses antibacterial and anti-inflammatory properties.[43–45] and a certain ability to promote osteogenic differentiation.[46,47] Based on prior investigations, the SCG-50% scaffold exhibited superior overall performance. Therefore, only the SCG-50% component was selected for drug loading. Furthermore, two drug concentration gradients were established: one with a high drug concentration (25 μM) component, denoted as SCG-50%-H, and the other with a low drug concentration (12.5 μM) component, denoted as SCG-50%-L. Taking high-concentration EGCG loading as an example, the specific steps were as follows. After considering previous swelling rate assessments (indicating equilibrium after 4 h of water absorption), the scaffolds of different compositions were immersed in EGCG solutions of varying concentrations. The scaffolds were sealed and left to stand for 4 h to ensure thorough absorption of EGCG. After 4 h, the scaffold was extracted with forceps, and the surface EGCG solution was rinsed away with deionized water. Drug loading was completed following the freeze-drying process.

2.6. Cell biocompatibility and proliferation

Samples of different components were prepared into 5 × 1 mm scaffolds, dried for 12 h, and then sterilized using ultraviolet irradiation for 24 h. Rat embryonic osteoblasts (MC3T3-E1; Beyotime, China) were cultured in high-glucose Dulbecco's Modified Eagle Medium in a carbon dioxide incubator until the third passage. Subsequently, the scaffolds were immersed in a cell suspension, removed after 2 h, and placed in a 96-well plate, where they were seeded with MC3T3-E1 cells at a density of 1×10^4 cells per well. The plate was incubated at 37°C for 1, 3, and 7 days. At each time point, a live/dead cell staining kit (Beyotime,China) was used on the scaffold surface (live cells appear green, dead cells appear red). After staining,

the cells were rinsed with phosphate-buffered saline, and scaffold surface cell adhesion was observed using an inverted fluorescence microscope (Axio Observer 7, ZEISS, Germany). Simultaneously, after ethanol dehydration, electron microscopy was used to observe the morphology of dead cells on the scaffold surface.

2.7. Cell counting kit-8 assay

Samples of different components were prepared into square scaffolds measuring 5 mm × 1 mm. The samples were dried in a vacuum oven for 12 h and then sterilized using ultraviolet irradiation for 24 h. The sterilized square scaffolds were submerged in the cell culture medium for 2 h. Subsequently, the cells were placed in a 24-well plate, and osteoblasts were seeded at a density of 5×10^4 cells per well. The plate was incubated in a carbon dioxide incubator for 1, 3, and 5 days, with media changes every 2 days. At each time point, a 10% cell counting kit-8 (Merck Millipore, Germany) solution was added to each well using a pipette, with care taken to avoid introducing bubbles into the wells, as these may interfere with the optical density readings. The plate was incubated in a carbon dioxide incubator for 1 h. The absorbance was measured at 450 nm using a microplate reader. Cell viability was calculated using **Equation (5)**. GraphPad statistical software (Graphpad Prism 9.5) was used for data analysis, plotting cell proliferation and cell viability graphs.

$$\text{Cell viability (\%)} = (a-c)/(b-c) \times 100 \quad (5)$$

where a is the absorbance of the wells of the microsphere scaffolds of different components of the experimental group, b is the absorbance of the control wells, and c is the absorbance of the blank.

2.8. *In vitro* osteogenic differentiation tests

Furthermore, in order to more accurately describe the osteogenic performance of the scaffold in vitro, we conducted co-culture of cells with the scaffold and performed alizarin red staining and ALP staining. The results are shown in Figures S8 and S9.

The supplementary section in the methodology is as follows:

The alkaline phosphatase (ALP) activity of the cells was assayed using an ALP kit (Beyotime, China). Rat embryonic osteoblasts (MC3T3-E1; Beyotime, China) were inoculated in 24-well plates with samples at a density of 5×10^4 cells/well. The cells were cultured for 1 day and then replaced with an osteoinductive solution to continue incubation for 3 and 7 days. ALP was then quantitatively characterized.

The calcium deposition on the scaffolds was evaluated using Alizarin Red S (ARS) staining (Beyotime, China). MC3T3-E1 were seeded in 24-well plates containing the scaffolds at a density of 5×10^4 cells/well. After 21 days of culture in an osteoinductive medium, the samples were washed twice with PBS, fixed in 4% paraformaldehyde for 30 minutes, and rinsed with distilled water. The fixed cells were then stained with 1% Alizarin Red S solution (pH 4.2) at room temperature for 30 minutes. After washing off excess dye with deionized water, the stained calcium nodules were imaged under a light microscope.

To assess the inhibitory or promotional effects of β-TCP and EGCG on the expression of osteogenic-related genes, SCG-50% and SCG-50%-L scaffolds were co-cultured with MC3T3-E1 for 7 days.

Relative expression of BMP2, RUNX2, COL1A1, OPN, and SP7 in SCG-50% and SCG 50%-L scaffolds after co-culture with MC3T3-E1 for 7 days.

2.9. Real-time quantitative polymerase chain reaction analysis

To assess the inhibitory or promotional effects of β-TCP and EGCG on the expression of osteogenic-related genes, SCG-50% and SCG-50%-L scaffolds were co-cultured with MC3T3-E1 for 7 days. Subsequently, the scaffolds were frozen in liquid nitrogen and ground, and Nucleo-ZOL (Macherey-Nagel, Germany) was employed to extract total cellular RNA. The Super-Mix reagent kit (Macherey-Nagel, Germany) was used to synthesize complementary DNA from total RNA through reverse transcription. A real-time polymerase chain reaction was conducted using the SYBR Green Master Mix reagent kit (Macherey-Nagel, Germany) to detect gene expression levels in the samples. To standardize the results, the $2^{-\Delta\Delta CT}$ method was applied to quantify gene expression levels. The primers used are detailed in **Table 2**.

2.10. *In vivo* tests

Rat cranial defects were used as models for large bone defects because they share similar bone healing mechanisms and challenges with large bone defects, and can be accurately replicated and observed in experimental animals.[48] Animal care and use procedures were approved by the Animal Ethics Committee of West China Hospital of Stomatology, Sichuan University, and followed all applicable institutional and governmental regulations regarding the ethical use of animals. The experimental manipulations were performed as follows. 12-week-old male Sprague–Dawley rats (n = 24, Dashuo, China) were anesthetized and shaved. Following that, a circular 5 mm defect was created in the rat skull using a dental ring drill, and the wound was sutured after implantation of

Table 2. Primer sequences

Gene	Forward primer	Reverse primer
Gapdh	5'-AATGTGTTCCGTCGTGGATCTG-3'	5'-CAACCTGGTCCTCAGTGTAGC -3'
Bmp2	5'-GGGACCCGCTGTCTTCTAGT-3'	5'-TCAACTCAAATTCGCTGAGGAC-3
Runx2	5'- GACTGTGGTTACCGTCATGGC -3'	5'ACTTGGTTTTTCATAACAGCGGA -3'
Col1a1	5'-TCGTGCCTAGCAACATGCC-3'	5'-ATTGGGGACCCTTAGGCCAT-3'
Sp7	5'-TCCCTGGATATGACTCATCCCT-3'	5'-CCAAGGAGTAGGTGTGTTGCC-3'

the sample. Postoperative antibiotics and cephalosporin antibiotics were injected daily for 3 consecutive days to prevent postoperative infection. The experiment was divided into five groups: Blank, SCG, SCG-50%, SCG-50%-L, and SCG-50%-H. Cranial samples were removed at 6 weeks and 12 weeks postoperatively, and the tissue was fixed with 4% paraformaldehyde. *In vivo* bone formation was scanned and analyzed using a computed tomography scanner (45 μCT; SCANCO Medical, Switzerland) with an X-ray voltage of 60 kV, a current of 500 μA, and an effective pixel size of 200 μm. Bone volume fraction (BV/TV) and bone mineral density (BMD) were calculated in the area of the bone defect using the Viscal software (version 2.1). The rat skull cap was subsequently decalcified for one month, embedded in paraffin, and sectioned at a thickness of 5 μm. The sections were fixed in xylene and stained with hematoxylin and eosin (H&E) and Masson's trichrome to visualize the tissue and bone structure.

2.11. Statistical analysis

The data were statistically and graphically analyzed using GraphPad Prism 8.0, and data analysis was performed using one-way analysis of variance. A p-value < 0.05 was considered significant (*p<0.05, **p<0.01, ***p<0.001, and ****p<0.0001).

2.12. Routine blood analysis.

At 12 weeks post-implantation, blood samples were collected from the retro-orbital venous plexus of the anesthetized rats into EDTA-anticoagulant tubes. The samples were immediately analyzed using an automatic hematology analyzer (Mindray BC-5000, Mindray, China) to evaluate systemic inflammation and biocompatibility. Key parameters, including white blood cell (WBC), red blood cell (RBC), and platelet (PLT) counts, were recorded to assess the host response.

3. Results and discussion

3.1. Characterization of the materialization properties of bioink

The gelation capability of hydrogels was assessed using the inversion method. The gelation capacity of different bioink components at various time intervals is depicted in Figure 2**A**. Following the addition of a fixed quantity of acidic 0.6% calcium chloride solution, the gel formation ability of the composite hydrogels gradually increased with prolonged crosslinking time. At 60 min of crosslinking time, hydrogels from all components were fully formed, showing no structural collapse even when tilted or inverted. Both the internal and external portions of the hydrogels were thoroughly crosslinked. This suggests that the use of acidic 0.6% calcium ions for crosslinking SA can lead to the formation of stable and uniform crosslinked hydrogels. Subsequently, the hydrogels crosslinked with acidic calcium ions were further crosslinked with 0.6% glutaraldehyde at 50°C for 3 h, followed by freeze-drying for 24 h, resulting in the fabrication of composite hydrogel materials.

To assess the emergence of new chemical groups and evaluate changes in group migration and bonding strength during the crosslinking and post-treatment processes of composite hydrogels, various samples were subjected to infrared spectroscopy analysis. The infrared spectra of the raw materials constituting the composite hydrogel are shown in Figure 2B. The vibrational absorption peaks of phosphate ions for β-TCP were observed at 551 cm^{-1} and 606 cm^{-1}, the asymmetric stretching vibration peak for P=O was observed at 1045 cm^{-1}, Gel showed characteristic peaks at 1651 cm^{-1} (C=O stretching vibration) and 1490 cm^{-1} (C–N stretching vibration), chitosan exhibited peaks at 2881 cm^{-1} (C–H stretching vibration) and 840 cm^{-1} (out-of-plane bending vibration of C–H), and SA had a symmetric stretching vibration peak for COO– group at 1414 cm^{-1}.

As depicted in Figure 2C, after composite formation and crosslinking between the materials, the characteristic peaks of each material remained, indicating that no new substances were generated during the crosslinking and post-treatment processes of the various component bioinks. However, changes in peak intensity and position were observed. Notably, after crosslinking with calcium ions, the carboxyl groups of SA were replaced by oxygen atoms closer to calcium ions, resulting in a noticeably weakened symmetric stretching vibration peak of the COO– group at 1414 cm^{-1}. This was a consequence of

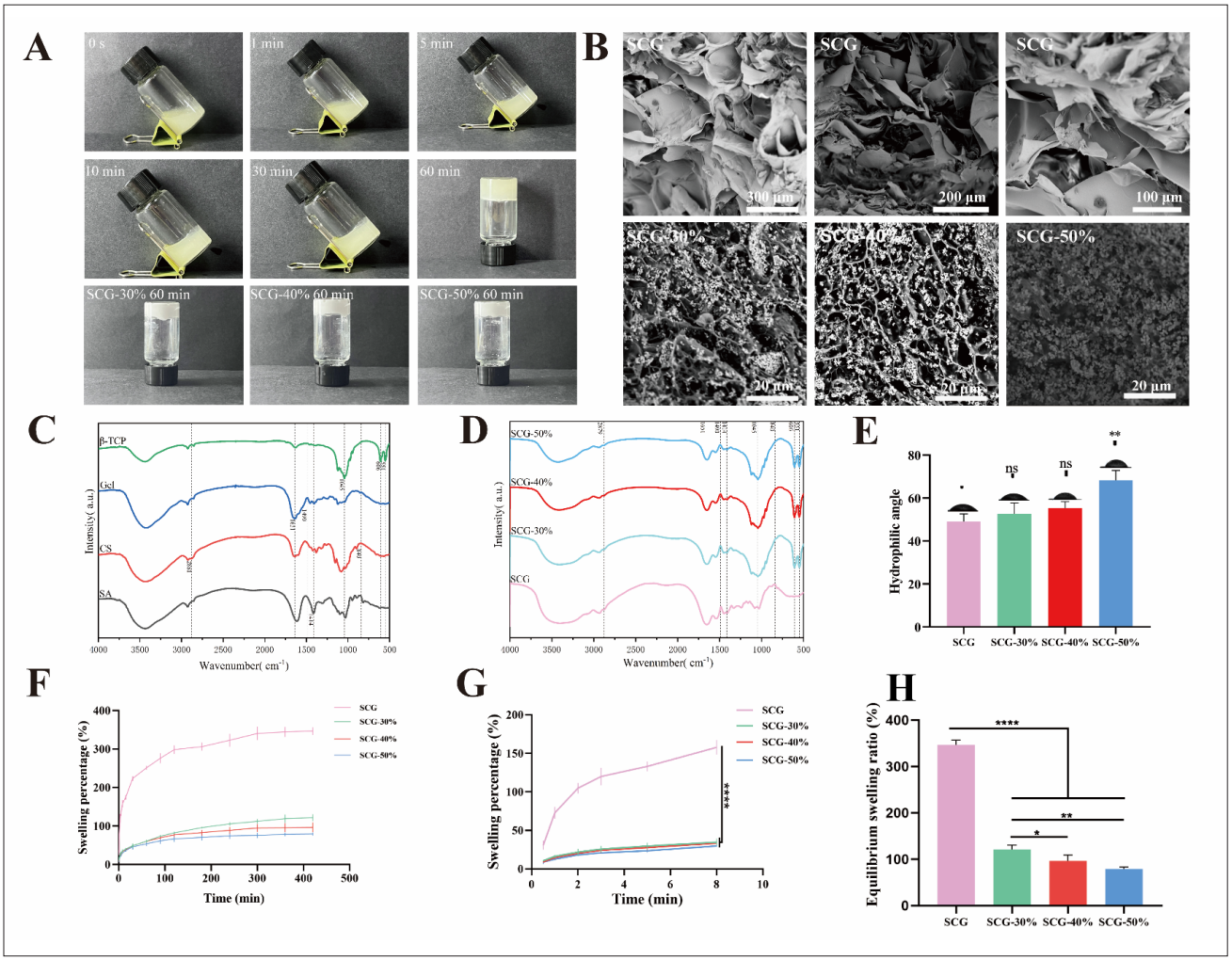

Figure 2. Basic characterization of bioink properties. (A) Schematic diagram of bioink gel capability. (B) Representative SEM images of SCG, SCG-30%, SCG-40%, and SCG-50%. (C) FTIR of sodium alginate (SA), chitosan (CS), gelatin (Gel), and β-tricalcium phosphate (β-TCP). (D) FTIR of SCG, SCG-30%, SCG-40%, SCG-50%, SCG-50%-L (low), and SCG-50%-H (high). (E) Hydrophilic angles of SCG, SCG-30%, SCG-40%, SCG-50%, SCG-50%-L, and SCG-50%-H films. (F) Change in swelling ratio of SCG, SCG-30%, SCG-40%, SCG-50%, SCG-50%-L, and SCG-50%-H composite hydrogels. (G) Change in swelling rate in each component for 8 min. (H) Comparison of equilibrium swelling ratio. Statistical significance determined at $^{*}p < 0.05$, $^{**}p < 0.01$, $^{***}p < 0.001$, and $^{****}p < 0.0001$; ns refers to not significant; n=3.

the formation of complexes between the carboxyl groups of polysaccharides, amino groups, and calcium ions. It was also notable that a new characteristic peak appeared at 1545 cm^{-1}. This was due to the vibration of the imine bond formed by the crosslinking of chitosan and Gel with glutaraldehyde, which manifested as a characteristic peak at approximately 1545 cm^{-1}. Additionally, the use of a crosslinking agent stabilized the crystal structure of β-TCP, leading to an increase in the intensity of the characteristic peak for phosphate ions. After crosslinking with glutaraldehyde, the intensity of the C=O group at 1651 cm^{-1} in the Gel decreased due to the reaction between the amino groups in the Gel and the aldehyde groups in glutaraldehyde, resulting in the formation of carboxylic acid condensation products. Consequently, the absorption peak of the C=O bond in Gel shifted to lower wavenumbers in the infrared spectrum. Moreover, changes in the absorption peak position of the C–N bond at 1490 cm^{-1} also occurred due to reactions between the amino groups in Gel and the aldehyde groups in glutaraldehyde. These changes robustly demonstrate the molecular interactions and good molecular compatibility between SA, chitosan, and Gel.

Hydrophilicity refers to the affinity of materials with hydrophilic groups for water molecules. Materials with strong hydrophilicity exhibit robust cell adhesion, and high hydrophilicity is advantageous for cell growth, reproduction, and fluid exchange. A smaller contact angle

indicates better hydrophilicity. After measuring the contact angle of the materials, the results, as shown in Figure 2D, reveal that the SCG pure hydrogel component exhibited strong hydrophilicity with an average contact angle of 49°. This is attributed to the presence of hydrophilic groups (hydroxyl & carboxyl groups) in the materials constituting the hydrogel. β-TCP is an inorganic material with relatively poor hydrophilicity compared to natural polymer materials. Consequently, with the addition of β-TCP, the contact angle gradually increased, indicating a decrease in hydrophilicity. When β-TCP was added up to 50%, the average contact angle was 68.33°. Although there was a trend of decreasing hydrophilicity with the addition of β-TCP, the contact angle remained below the hydrophilic–hydrophobic threshold of 90°, indicating that this inorganic salt–gel system exhibited good hydrophilicity, which may facilitate cell adhesion and proliferation.

The swelling rate calculation was employed to assess the water absorption and swelling properties of composite hydrogel materials over a specified duration. Composite hydrogel materials exhibiting a higher swelling rate demonstrate enhanced fluid exchange capabilities, facilitating cellular interactions and substance transport. Nevertheless, research indicates that when applied in bone tissue repair, especially in the restoration of spinal and cranial injuries, excessive swelling can lead to deformation and expansion of the hydrogel, exerting pressure on nerves. Moreover, a higher swelling rate significantly compromises the mechanical properties. Therefore, it is crucial to control the swelling characteristics of hydrogel substrates. The results of swelling rate measurements, as depicted in Figure 2E, reveal the outstanding swelling properties of the SCG group, reaching equilibrium at approximately 300 min with a swelling rate of 340.52%. Upon the addition of β-TCP, there was a notable reduction in the equilibrium swelling rate, accompanied by an extended time to reach equilibrium. Specifically, the SCG-50% sample took approximately 360 min to achieve equilibrium swelling, and the equilibrium swelling rate decreased to 73.99%.

Figure 2F illustrates the variations in short-term swelling rates for samples with different compositions. The SCG group exhibited rapid swelling, while samples containing β-TCP showed diminished but still rapid swelling capabilities, reaching approximately 40% swelling within 8 min. In Figure 2G, a statistical analysis of the equilibrium swelling rates of composite hydrogels for each component demonstrates that the inclusion of β-TCP significantly inhibited the swelling behavior of the hydrogel. As the quantity of β-TCP increased, the equilibrium swelling rate consistently decreased. Therefore, the addition of β-TCP allowed for the regulation of the swelling rate of SCG hydrogels, effectively suppressing excessive swelling behavior.

3.2. Scaffold fabrication and characterization

To enhance the high-level formability of the scaffold, a pre-crosslinking approach was employed to augment the viscosity of the bioink. Throughout this process, varying concentrations of calcium ions were employed at 0.2%, 0.4%, 0.6%, and 0.8% w/v, following a bioink-to-calcium ion ratio of 2:0.1 (v/w). The evaluation criteria encompassed the extrusion behavior of the bioink and the formability of the scaffold. As depicted in Figure 3A, the results indicate that the scaffold exhibited optimal formability when the pre-crosslinking calcium ion concentration was 0.6%. This superiority was attributed to the synergistic interplay of multiple factors. Primarily, pre-crosslinking, by elevating the viscosity of the scaffold, ensured the accuracy of filamentous shape retention during the extrusion process of the bioink. Simultaneously, rapid solidification of the thermosensitive Gel was facilitated by the use of a cold plate, enabling better shaping of the bottom layer of the scaffold. Conversely, in the absence of pre-crosslinking treatment, the lower viscosity of the bioink resulted in poor continuity of extrusion, leading to structural collapse and deformation issues during the printing process. Through pre-crosslinking, we successfully heightened the viscosity of the bioink, ensuring a more uniform and stable extrusion. Furthermore, due to the enhanced viscosity, the formability of the scaffold was significantly augmented, mitigating issues of collapse. This experimental outcome unequivocally underscores the necessity and efficacy of the pre-crosslinking strategy. Furthermore, we verified the printing performance of the ink through rheological analysis. Through oscillation experiments, it was observed that SCG and SCG-50% exhibited higher moduli at low strains, while the ink modulus decreased under high strain application, accompanied by a recovery of the strain recovery modulus, indicating that the printed ink can be extruded and reformed under the shear thinning effect (Figure S2).

Following the completion of pre-crosslinking, scaffolds with varying β-TCP content were fabricated using an extrusion-based 3D bioprinting system. Subsequently, after crosslinking with acidic calcium ions and glutaraldehyde, the scaffolds underwent freeze-drying to achieve the final form. Figure 3B illustrates the states of the scaffolds at different stages. After acidic calcium ion crosslinking, the morphology of the scaffolds remained unchanged, while an increase in hardness was observed. However, following glutaraldehyde crosslinking, the color of the scaffold changed to pale yellow. This phenomenon resulted from the Schiff base reaction between Gel and

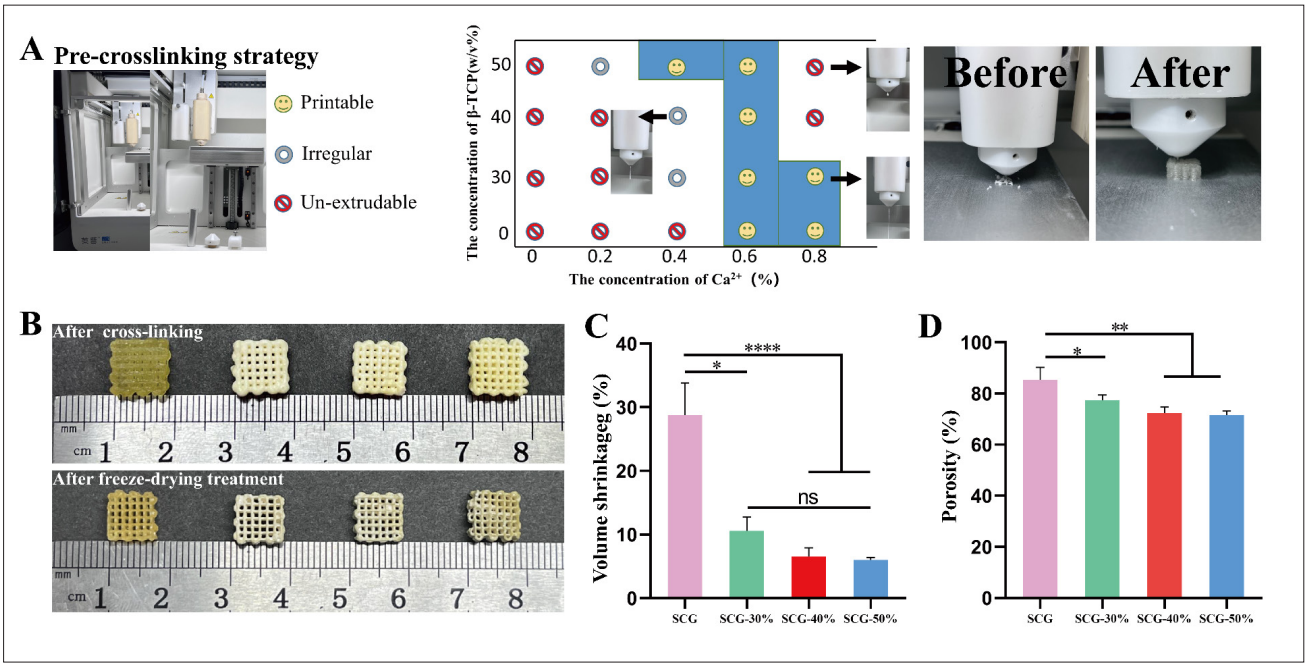

Figure 3. Printing and characterization of scaffolds. (A) Determination of pre-crosslinking effect and concentration. (B) Changes in macroscopic morphology of scaffolds during post-treatment. (C) Volume shrinkage of SCG, SCG-30%, SCG-40%, and SCG-50% scaffolds before and after freeze-drying. (D) Porosity of SCG, SCG-30%, SCG-40%, and SCG-50% scaffolds. Statistical significance determined at $^{*}p < 0.05$, $^{**}p < 0.01$, $^{***}p < 0.001$, and $^{****}p < 0.0001$; $n=3$. Abbreviation: β-TCP, β-tricalcium phosphate; ns, not significant.

glutaraldehyde, leading to the formation of a crosslinked structure that altered the conformation and charge state of Gel molecules, influencing light absorption and scattering characteristics and thus causing a change in the scaffold color. Simultaneously, the crosslinking action further increased the scaffold's hardness and induced the formation of a double network structure with interpenetrating crosslinks within the interior. Finally, after freeze-drying, the removal of internal ice crystals significantly improved the varying degrees of contraction in the scaffold, resulting in a roughened surface. Concomitantly, the mechanical properties of the scaffold significantly improved. The outcomes of these sequential preparation steps reflected changes in the structure and performance of the scaffold at different stages, providing crucial information about its effectiveness in biomedical applications.

Upon conducting statistical analyses on the volume shrinkage rates of scaffolds with different β-TCP contents before and after freeze-drying, as depicted in Figure 3C, the volume shrinkage rate of the pure water gel scaffold was found to be 28.79%. Undoubtedly, this would adversely affect the precision of scaffold applications. However, with the addition of β-TCP, the volume shrinkage rates of the scaffolds decreased to 10.57%, 6.55%, and 6.01%, respectively. There was a significant difference in the volume shrinkage rates between the pure water gel scaffold and those incorporating β-TCP. This observation underscores that the inclusion of β-TCP markedly enhances the shape stability and fidelity of the scaffold before and after freeze-drying.

This improvement is attributed to the uniform attachment of β-TCP to the network structure of the water gel scaffold. This attachment effectively impeded the volume shrinkage of the water gel during freeze-drying, maintaining the stability of the scaffold shape. The incorporation of β-TCP has been proven instrumental in preserving the structural integrity of scaffolds during the freeze-drying process.

The results of the application of the Archimedes drainage method for measuring scaffold porosity are presented in Figure 3D. The porosity of the pure water gel scaffold reached a high value of 85.33%. However, upon the addition of β-TCP, the scaffold porosity significantly decreased to 77.37%, 72.33%, and 71.64%, respectively. It is noteworthy that the porosity of trabecular bone in the human body typically ranges between 70% and 90%. Thus, the porosity of the prepared scaffolds met the requirements for trabecular bone. Importantly, the pure water gel composition exhibited a significant difference in porosity compared to the other groups. This further underscores

that the addition of β-TCP significantly enhances the shape fidelity of the scaffold during post-processing. This has crucial implications for the biocompatibility and performance of the scaffold, especially in bone tissue engineering and medical applications, where scaffold porosity can influence cell adhesion and bone tissue growth. Therefore, these results highlight the advantages of incorporating β-TCP, with the potential to improve scaffold performance, making it more suitable for bone tissue repair and biomedical applications.

3.3. Microscopic morphological characterization of scaffold cross-sectional surface

Figure 4A shows the SEM images of the surfaces of the SCG, SCG-30%, SCG-40%, and SCG-50% scaffolds. The SEM results reveal that the surface of the SCG pure hydrogel scaffold was smooth and devoid of micropores, a result of the crosslinking process, underscoring the thoroughness of scaffold crosslinking. Conversely, upon the introduction of β-TCP, the scaffold surface undergoes a transformation due to the incorporation of β-TCP into the hydrogel, resulting in a roughened texture and a porous state. This morphological alteration, characterized by a rough surface, proves advantageous for cell adhesion and growth on the scaffold surface. The presence of surface micropores further facilitates the transport of nutrients and the exchange of substances within bodily fluids. The integration of β-TCP not only altered the surface topography but also enhanced the scaffold's biocompatibility, rendering it conducive to cellular activities and promoting efficient material exchange at the interface of the scaffold and the biological milieu. These findings underscore the pivotal role of β-TCP in modulating the structural and functional characteristics of the scaffold surface, thereby influencing its performance in tissue engineering applications.

Figure 4B presents the SEM images of the cross-sections of SCG, SCG-30%, SCG-40%, and SCG-50% scaffolds. The SEM images distinctly reveal that the cross-sections of all scaffold components exhibited a continuous network of porous structures after freeze-drying. Upon closer examination of the cross-sectional SEM results of the SCG pure hydrogel scaffold, it was evident that the polymer network of the pure hydrogel underwent contraction and adhesion between polymer strands after the freeze-drying process. This resulted in a decrease in the shape fidelity of the scaffold, accompanied by an enlargement of pores compared to other components. This microscopic

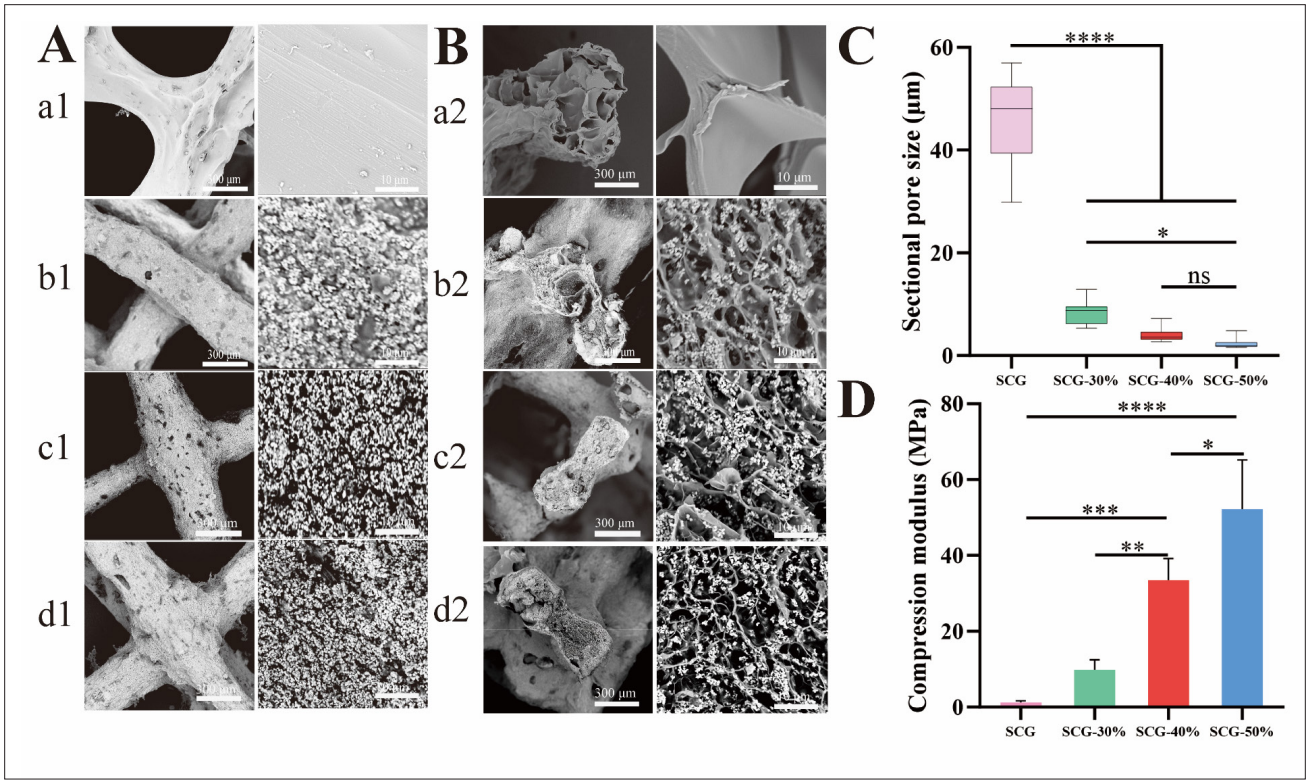

Figure 4. Microstructure morphology and related performance characterization of scaffolds with different components. (A) Surface morphology of scaffolds. Scale bars: 10 μm, 300 μm; magnifications: 15×. (B) Cross-sectional morphology of scaffolds. Scale bars: 10 μm, 300 μm; magnifications: 15×. (C) Analysis of the cross-sectional aperture of the scaffold. (D) Compression modulus of scaffolds. Statistical significance determined at $^{*}p < 0.05$, $^{**}p < 0.01$, $^{***}p < 0.001$, and $^{****}p < 0.0001$; ns refers to not significant; n=3.

observation elucidates the reasons for the volume shrinkage of the scaffold before and after post-processing. With the addition of β-TCP, it adhered uniformly to the 3D crosslinked network structure. This uniform adhesion, combined with the hydration process of ceramic materials, ensured that a high degree of fidelity is maintained within the 3D structure of the composite scaffold. Moreover, the close integration of β-TCP with the hydrogel network enhanced the mechanical properties of the scaffold. At the same time, we also printed scaffolds SCG-60% and SCG-70% with higher β-TCP content. The electron microscopy results are shown in Figure S3. The inside of the scaffold was filled with β-TCP, resulting in the loss of its bionic structural organization.

Subsequently, the Nano Measurer software was employed to statistically analyze the micropore sizes on the cross-sections of the scaffolds. The statistical results revealed that the micropore diameter of the cross-sections of the SCG pure hydrogel scaffold was approximately 50 μm, displaying a significant difference compared to other components. The micropore sizes on the scaffold cross-sections exhibited a decreasing trend with the gradual addition of β-TCP. The analysis in Figure 4C further explores the distribution of micropore sizes on the cross-sections of various components, indicating that the micropores in the scaffold with added β-TCP were distributed in the range of 1–20 μm. This size range was comparable to the pore sizes between trabeculae in cancellous bone, suggesting that the scaffold possesses a biomimetic internal structure.

Following compression modulus testing of the scaffolds using a universal testing machine, the results depicted in the graph (Figures 4D and S4) indicate that the average compression modulus of the SCG pure hydrogel scaffold was 1.25 MPa. In contrast, the SCG-30% scaffold exhibited an average compression modulus of 9.80 MPa, SCG-40% had an average compression modulus of 33.50 MPa, and SCG-50% demonstrated an average compression modulus of 52.22 MPa. Furthermore, we also conducted compression tests on the scaffolds in a humid environment. The test results showed that the compression modulus of the SCG scaffold was only 111.5 ± 5.24 kPa. However, after adding β-TCP, the compression modulus of the SCG-50% scaffold increased to 1080.75 ± 62.30 kPa (Figure S5). The inclusion of β-TCP in the scaffolds aligns with the compressive modulus requirements of cancellous bone. Significant differences were observed between the SCG pure hydrogel component and the components with added β-TCP, suggesting a substantial enhancement in the mechanical strength of the scaffold upon the addition of β-TCP. Moreover, the compression modulus showed an increasing trend with increasing β-TCP content. The primary reason for this change is the uniform attachment of β-TCP to the hydrogel network, reinforcing the hydrogel scaffold's ability to resist deformation.

3.4. *In vitro* degradation performance analysis

After subjecting the scaffolds to degradation for 2, 4, and 8 weeks, we conducted a comprehensive analysis of the degradation rates, changes in the degradation fluid pH, variations in the scaffold's compressive modulus, and morphological characteristics of scaffolds with different components. First, as shown in Figure 5A, after a period of degradation, the surface of each scaffold showed apparent changes. The SCG pure hydrogel component scaffold exhibited the most significant change, and fractures were observed on its surface. This was due to the instability of SA during the degradation process, resulting in uncrosslinking and leading to phase separation between polymers. This phenomenon was more evident after 8 weeks of degradation. For scaffolds with β-TCP added, the scaffold surface rarely broke, but instead formed smooth, crater-like depressions due to the continuous release of calcium ions from β-TCP during the degradation process, which can enhance inter-tissue communication. The adhesive was continuously crosslinked with SA to ensure the stability of the scaffold. As depicted in Figure 5B, we observed variations in the degradation rate (mass loss rate) of the scaffolds at different time points. The results revealed that in the 2nd week, all scaffold components exhibited noticeable degradation behavior. Notably, scaffolds composed of SCG pure hydrogels displayed the most rapid degradation, with a mass loss rate of up to 10%. By week 4, the degradation rate of these scaffolds further increased to 15%. Concerningly, by the 8-week mark, structural collapse of the scaffolds occurred, resulting in degradation rates reaching approximately 25%.

In contrast, scaffolds doped with β-TCP maintained morphological stability throughout the degradation process and effectively reduced the degradation rate. At the 8-week time point, the degradation rate of these scaffolds did not exceed 20%. Importantly, it was observed that the degradation rates of scaffolds with different components were significantly influenced by the β-TCP content. This observation indicates that the addition of β-TCP distinctly modulates the degradation behavior of the scaffolds. This effect can be attributed to the hydration reaction of β-TCP bioceramics during degradation, which led to the gradual release of calcium ions, thereby preserving the structural stability of the hydrogel components.

The variation in pH levels of the degradation fluid during the scaffold degradation process plays a pivotal role in determining whether an inflammatory response occurs within the organism. Consequently, we conducted a comprehensive assessment of the pH levels in the

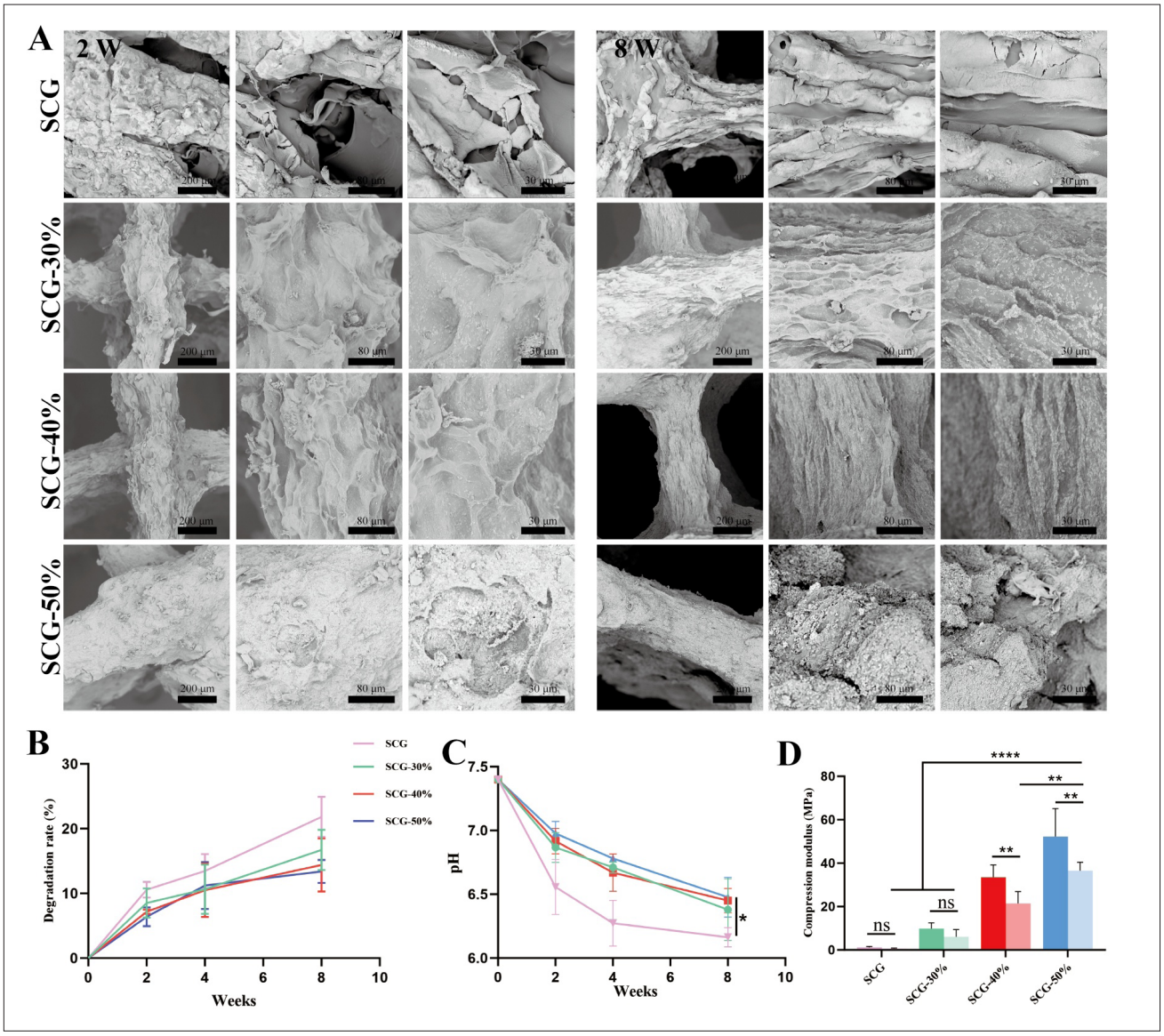

Figure 5. Performance changes of scaffolds with different components during *in vitro* degradation. (A) The micromorphology of the SCG, SCG-30%, SCG-40%, and SCG-50% scaffolds changed after 2 and 8 weeks of degradation. Scale bars: 30 μm, 80 μm, 200 μm; magnifications: 20×. (B) Degradation rate of different components of scaffolds. (C) Changes in degradation cycle pH. (D) Compression modulus changes of scaffolds after 8 weeks of degradation of SCG, SCG-30%, SCG-40%, and SCG-50% scaffolds. (E) Compression modulus loss rate of each component scaffold after 8 weeks of degradation, Statistical significance determined at $^{*}p < 0.05$, $^{**}p < 0.01$, $^{***}p < 0.001$, and $^{****}p < 0.0001$; ns refers to not significant; n=3.

degradation fluid. As illustrated in Figure 5C, we observed pH variations at different time points for various β-TCP scaffolds. The results revealed a discernible declining trend in pH values during the scaffold degradation process. Notably, the pH value of the pure hydrogel scaffolds had already plummeted to below 6.5 by week 4. This decline can be attributed to the hydrolysis process of the Gel, wherein peptide chains progressively unfold, break apart, and ultimately degrade into smaller peptide chains, such as collagen. Typically, the pH of collagen falls within the range of 6.0 to 7.5, and pH values within this range generally do not adversely affect the acid-base balance of an animal's body, nor do they impact the adhesion properties of human cells or cellular metabolism. Conversely, the pH values of scaffolds incorporating β-TCP remained relatively stable, hovering at approximately 6.5 after 8 weeks of degradation. This outcome signifies that the addition of β-TCP markedly ameliorated the declining pH trend during the degradation process, aligning with the degradation behavior trend. Consequently, it can be inferred that β-TCP scaffolds contribute to the maintenance of an acid-base equilibrium in the surrounding scaffold environment during

degradation. This holds promising prospects for mitigating the risk of unnecessary inflammatory responses within the organism, thereby bearing significant positive implications for the biomedical application of such scaffolds.

The loss of the scaffold's compressive modulus due to degradation is inevitable. The compressive modulus of the scaffold, both before and after degradation, is presented in Figure 5D. This figure compares the compressive modulus of the scaffold after 8 weeks of degradation with its initial compressive modulus. From the results, it is evident that scaffolds with different components all exhibited a significant decline in their compressive modulus after degradation, with notable differences among them. As shown in Figure 5E, after a period of degradation, the compressive modulus attenuation rate for the SCG-50% component scaffold was 30.12%, 35.64% for the SCG-40% component scaffold, 37.76% for the SCG-30% component scaffold, and 48.8% for the SCG component scaffold. Thus, the addition of β-TCP significantly reduced the attenuation of the compressive modulus of the scaffold during the degradation process, thereby enhancing the stability of the scaffold's structure and mechanical properties.

In summary, these findings underscore the significant enhancement of structural stability and effective regulation of degradation behavior in scaffolds achieved through the incorporation of β-TCP. These results hold crucial implications for the long-term stability and performance of scaffolds in biomedical applications.

3.5. *In vitro* mineralization capability analysis

In the realm of bone tissue engineering scaffolds, materials endowed with robust *in vitro* mineralization capabilities can facilitate the formation of stable inorganic compound layers on their surfaces. This distinctive attribute enhances the biocompatibility and mechanical performance of the materials, thereby promoting the scaffold's integration with the surrounding tissue. Consequently, it expedites the rehabilitation and growth of compromised bone tissue.

As depicted in Figure 6, SEM images showed the formation of hydroxyapatite-like layers on the surfaces of scaffolds SCG, SCG-30%, SCG-40%, and SCG-50% during cultivation periods of 3, 7, and 14 days in a simulated body fluid, firmly adhering to the scaffold surfaces. Moreover, an explicit trend emerged with prolonged incubation time, where the hydroxyapatite-like layer particles exhibited gradual enlargement, accompanied by an outward expansion tendency. These *in vitro* mineralization experiments unequivocally underscore the remarkable *in vitro* mineralization capacity inherent to these scaffold materials. Furthermore, we conducted X-ray diffraction analysis on the mineralized scaffolds, and the results revealed characteristic peaks of hydroxyapatite, confirming the success of the mineralization process (Figure S6).

3.6. *In vitro* biocompatibility

Good biocompatibility is a crucial condition for implantable stents. At the same time, the addition of active factors is required to accelerate the bone regeneration cycle. EGCG was loaded through the swelling effect of the stent. We measured the drug release rate of EGCG. The results showed that the release rate of EGCG was slow over the first 14 days, thereby achieving a good sustained-release effect (Figure S7).

Figure 7 presents the experimental results of the scaffold *in vitro* cell culture. The outcomes, depicted in Figure 7A, reveal that during the initial phase, on the 1st day of cultivation, minimal attachment of MC3T3-E1 cells was observed on the scaffold surfaces, indicating relatively low cell adhesion. However, as the cultivation period extended, the cell population on the scaffold surfaces rapidly increased. By day 7, the scaffold surfaces were completely covered by cells, signifying an optimal cellular growth environment provided by the scaffold. Notably, the results of live/dead cell staining distinctly indicated an abundance of viable cells on the scaffold surfaces, underscoring the scaffold's compatibility with cells. This observation underscores the scaffold's ability to support cell viability, a crucial attribute in evaluating its biocompatibility for potential applications in tissue engineering and regenerative medicine.

For a more in-depth understanding of the cellular status on scaffold surfaces, scaffolds cultivated for 7 days were subjected to ethanol dehydration treatment and subsequently observed under SEM at various magnifications. Figure 7B represents the surface morphology of scaffolds SCG, SCG-30%, SCG-40%, SCG-50%, SCG-50%-L, and SCG-50%-H, respectively, with different compositions. Through electron microscopy images, a clear depiction of the morphology and structure of cells on the scaffold surfaces was discernible.

In comparison to the scaffold composed of pure water gel, the surfaces of scaffolds incorporating β-TCP exhibited a rougher and more porous microstructure. This microscopic structural characteristic facilitated better adhesion of cell pseudopodia onto the micropores on the scaffold surface. This feature provided increased surface area and opportunities, aiding in cell attachment and growth on the scaffold surface. Importantly, this observation adds supplementary support and explanation for the enhanced cell compatibility of the scaffold, as it offers additional surface features conducive to cell adhesion and growth.

According to the data presented in Figure 7C, absorbance measurements were conducted to assess cell

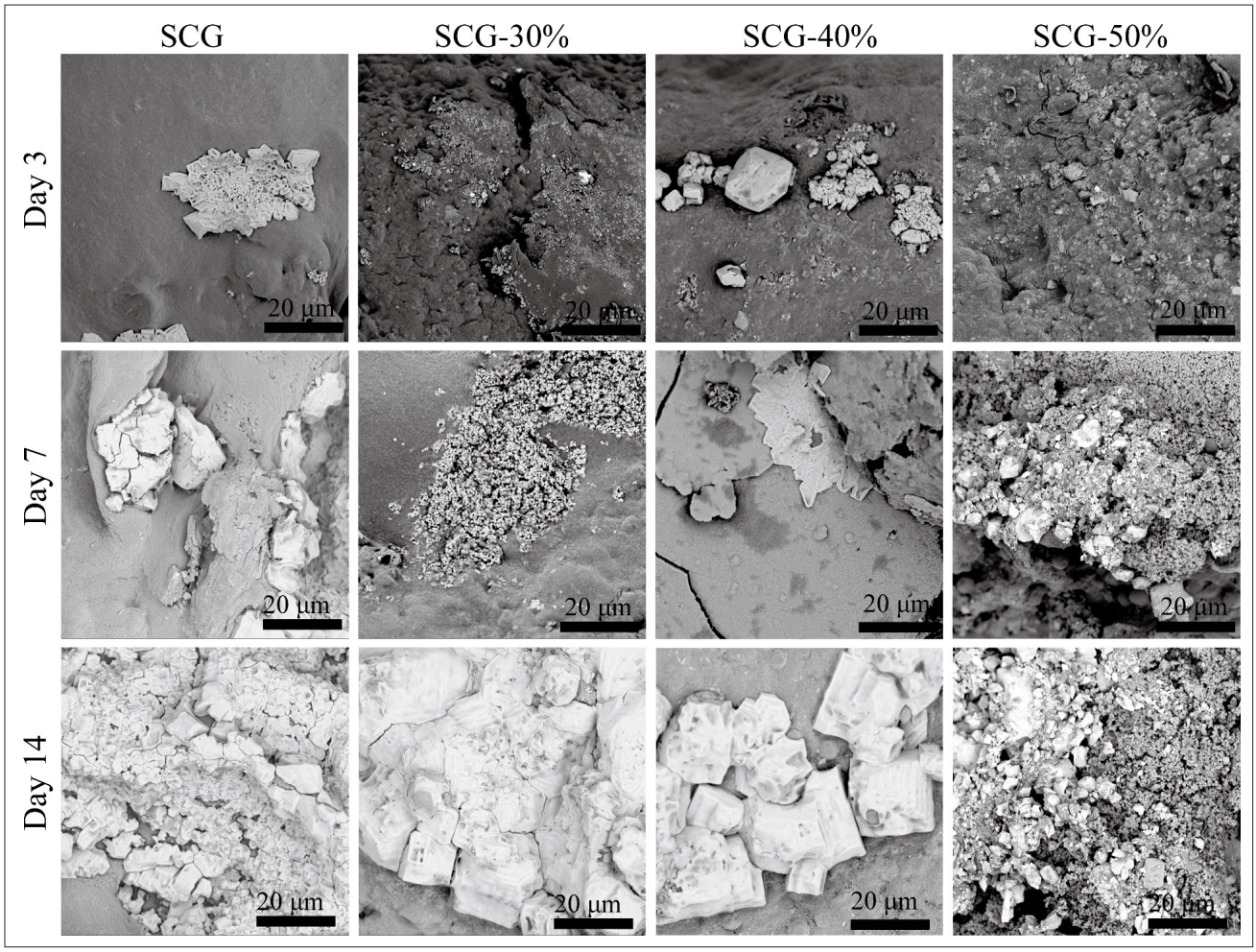

Figure 6. The formation of a hydroxyapatite-like layer on the scaffold surface after days 3, 7, and 14 of mineralization in the simulated body fluid. Scale bar: 20 μm; magnification: 40×.

proliferation on scaffolds with different compositions. Initially, on the 1st day, the absorbance values (optical density values) for each group were similar, indicating a relatively consistent impact of the scaffolds on cells at the initial stage. However, as the cultivation time extended to the 3rd day and 5th day, we observed that the absorbance values for the experimental groups were significantly higher than those of the control group. Scaffolds incorporating β-TCP exhibited notable differences, indicating a significant enhancement of cell proliferation due to the addition of β-TCP. Furthermore, the absorbance of scaffolds loaded with EGCG was markedly higher than that of other compositions, indicating that the addition of EGCG contributes to a more effective promotion of cell proliferation. The SCG-50%-L composition demonstrated particularly outstanding promotion effects, while the effects of the SCG-50%-H composition were relatively weaker, possibly due to the cytotoxicity associated with the higher concentration of EGCG. The calculated cell viability rates were further illustrated, showing that the cell viability rates for all scaffold compositions exceeded 100%. This outcome aligns with the absorbance trends, indicating that scaffolds from all compositions were nontoxic to cells. Moreover, scaffolds containing β-TCP components exhibited superior cell viability rates, with scaffolds loaded with a low concentration of EGCG exerting the most significant impact on cell viability.

The addition of β-TCP significantly promoted cell proliferation, and the incorporation of EGCG had a positive influence on cell proliferation. These findings provide robust scientific evidence for the biocompatibility and cell adhesion of the scaffolds.

As depicted in Figure 7D, we conducted a study on ALP activity, a characteristic enzyme within osteoblasts. On day 7 of cultivation, the ALP activities for scaffolds

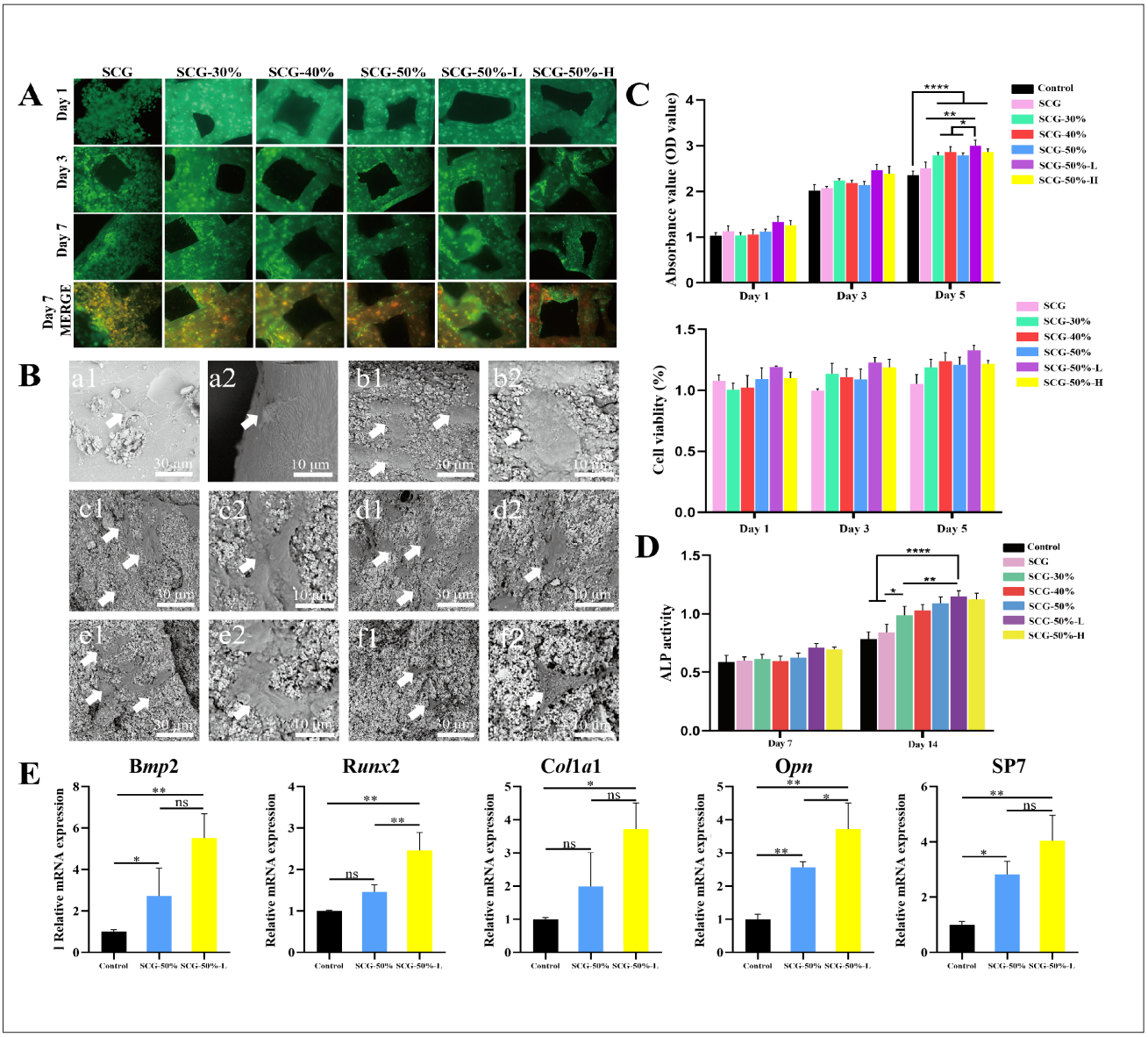

Figure 7. Cell compatibility and expression of osteogenic-related genes in scaffolds with different compositions. (A) Staining of SCG, SCG-30%, SCG-40%, SCG-50%, SCG-50%-L (low), and SCG-50%-H (high) scaffolds on the surface of scaffolds co-cultured with rat embryonic osteoblasts for 7 days. (B) Morphology of dead cells on the surface of SCG (a1 & a2), SCG-30% (b1 & b2), SCG-40% (c1 & c2), SCG-50% (d1 & d2), SCG-50%-L (e1 & e2), and SCG-50%-H (f1 & f2) scaffolds after co-culture for 7 days. Scale bars: 10 μm, 30 μm; magnifications: 40×. (C) Optical density (OD) values of cell proliferation and cell survival rate of SCG, SCG-30%, SCG-40%, SCG-50%, SCG-50%-L, and SCG-50%-H scaffolds at days 1, 3, and 5. (D) Alkaline phosphatase (ALP) activity of different components of scaffolds at days 7 and 14. (E) Relative expression of *BMP2*, *RUNX2*, *COL1A1*, *OPN*, and *SP7* in SCG-50% and SCG-50%-L scaffolds after co-culture with mesenchymal stem cells for 7 days. Statistical significance determined at $^{*}p < 0.05$, $^{**}p < 0.01$, $^{***}p < 0.001$, and $^{****}p < 0.0001$; ns refers to not significant; n=3.

from different compositions were relatively similar, indicating a comparable impact of the scaffolds on osteoblast activity at the initial stage. However, as the cultivation period extended to day 14, the difference in ALP activity between scaffolds loaded with β-TCP and the SCG pure water gel scaffold significantly increased. This result unequivocally indicates that the addition of β-TCP significantly influences and enhances the activity of ALP, providing clear support for the osteogenic function of bone cells. Moreover, compared to other compositions, the SCG-50%-L scaffold exhibited significantly higher ALP activity, suggesting that low concentrations of EGCG have a more potent promoting effect on ALP activity. This finding reveals the crucial role of EGCG in enhancing the osteogenic function of bone cells within the scaffold. Therefore, this research not only underscores the benefits

of β-TCP but also highlights the potential application prospects of low-concentration EGCG, bearing significant scientific implications for the advancement of bone tissue engineering and regenerative medicine.

The primary focus of this experiment was to examine the gene expression of SCG-50% and SCG-50%-L scaffolds, with the aim of exploring the corresponding gene expression in scaffolds containing β-TCP and EGCG. The expression of five genes was analyzed after day 7 of cultivation. These genes include recombinant human bone morphogenetic protein-2 (*BMP2*), runt-related transcription factor 2 (*RUNX2*), alpha-1 type I collagen (*COL1A1*), which promotes the formation of connective tissue, osteopontin (*OPN*), which is closely associated with bone formation and development, and zinc finger transcription factor (*SP7*), which promotes the differentiation of osteoblasts into mature osteoblasts and bone cells. The results, as depicted in Figure 7E, reveal significant expression of the detected genes, indicating that the composite scaffolds can better promote the expression of genes related to osteogenesis. Moreover, the relative gene expression levels of the scaffolds loaded with EGCG were higher than those without EGCG, demonstrating the osteogenic-promoting function of EGCG.

At the same time, to better characterize the *in vitro* osteogenic performance of the scaffold, we examined calcium deposition and cytoskeletal morphology, and performed alizarin staining and cytoskeletal staining. The results are shown in Figures S8 and S9.

3.7. The *in vivo* osteogenic effects of the scaffolds

All rats survived after scaffold implantation, and no rejection or inflammation was found in subsequent feedings. The weight changes of the rats are shown in Figure S10**.** At the same time, we conducted a routine blood assessment and found that all rats in all groups exhibited an increase in inflammatory indicators (Figures S11 & S12). The scaffold was removed at different time points, as shown in Figure S13**.** The 3D reconstructions of micro-computed tomography scans at different time points (6 weeks and 12 weeks) depicting the bone defect sites are illustrated in Figure 8A. It is evident from the images that at week 6, the blank control group exhibited minimal new bone formation, whereas the macroscopic osteogenic efficiency of the SCG-50%, SCG-50%-L, and SCG-50%-H groups surpassed that of the pure hydrogel and blank control groups. To further elucidate the observed outcomes, quantitative analysis was conducted. As shown in Figure 8B, at the 6th week, the BV/TV ratio for the blank control group was only 5.18%, whereas the SCG group presented a BV/TV value of 8.03%. At the same time, we found that in complex humoral environments, SCG scaffolds have undergone structural collapse and dispersion. SCG-50% demonstrated a BV/TV value of 13.03%, and the SCG-50%-L scaffold, incorporating EGCG, exhibited optimal osteogenic performance with a BV/TV value of 18.59%. The scaffold loaded with a high concentration of drug, SCG-50%-H, achieved a BV/TV value of 17.48%. By the 12th week, the BV/TV values for all scaffold components showed a significant increase. Notably, the SCG-50%-L component displayed the most favorable reparative effects, attaining a BV/TV value of 23.40%, surpassing both the SCG group (9.10%) and the SCG-50% group (15.73%). The BV/TV values at different time points suggest that the addition of β-TCP effectively promoted new bone formation, and EGCG demonstrates a pronounced enhancement in osteogenesis.

As depicted in Figure 8C, the BMD values of various scaffold components at different time intervals are illustrated. At week 6, the BMD for the blank control component was 73.89 mg HA/ccm, the SCG component exhibited a BMD value of 160.52 mg HA/ccm, and the SCG-50% component had a BMD value of 201.17 mg HA/ccm. Notably, the SCG-50%-L component, featuring a low drug concentration, achieved the highest bone density with a BMD value of 247.99 mg HA/ccm, while the high drug concentration SCG-50%-H component showed a relatively lower BMD value of 224.18 mg HA/ccm compared to the low drug concentration counterpart. By the 12th week, a noticeable increase in bone density was observed for all scaffold components. Remarkably, the SCG-50%-L component exhibited the highest bone density, with a BMD value soaring to 290.86 mg HA/ccm, and the other components also demonstrated substantial growth. The BMD values mirror the trends observed in BV/TV values, indicating that the addition of β-TCP significantly promotes new bone formation, and EGCG exhibits a marked enhancement in osteogenesis.

In the 12th week, tissue histological analysis was conducted on decalcified tissues to further assess the bone formation process (Figure 9A). According to the H&E staining results at week 12, a significant amount of fibrous tissue was observed in the bone defect area, indicating the presence of a self-repair mechanism. Simultaneously, scaffolds loaded with β-TCP exhibited a stronger new bone-inducing effect. The newly formed bone tissue exhibited a bridging interface with the original bone, and drug-loaded scaffolds demonstrated enhanced bone-inducing and bone-integrating capabilities.

Masson staining stains dense collagen fibers, muscle fibers, and red blood cells red, while loose collagen fibers and cellulose are stained blue. As shown in Figure 9B, bone tissue appeared blue, indicating that the rat cranial

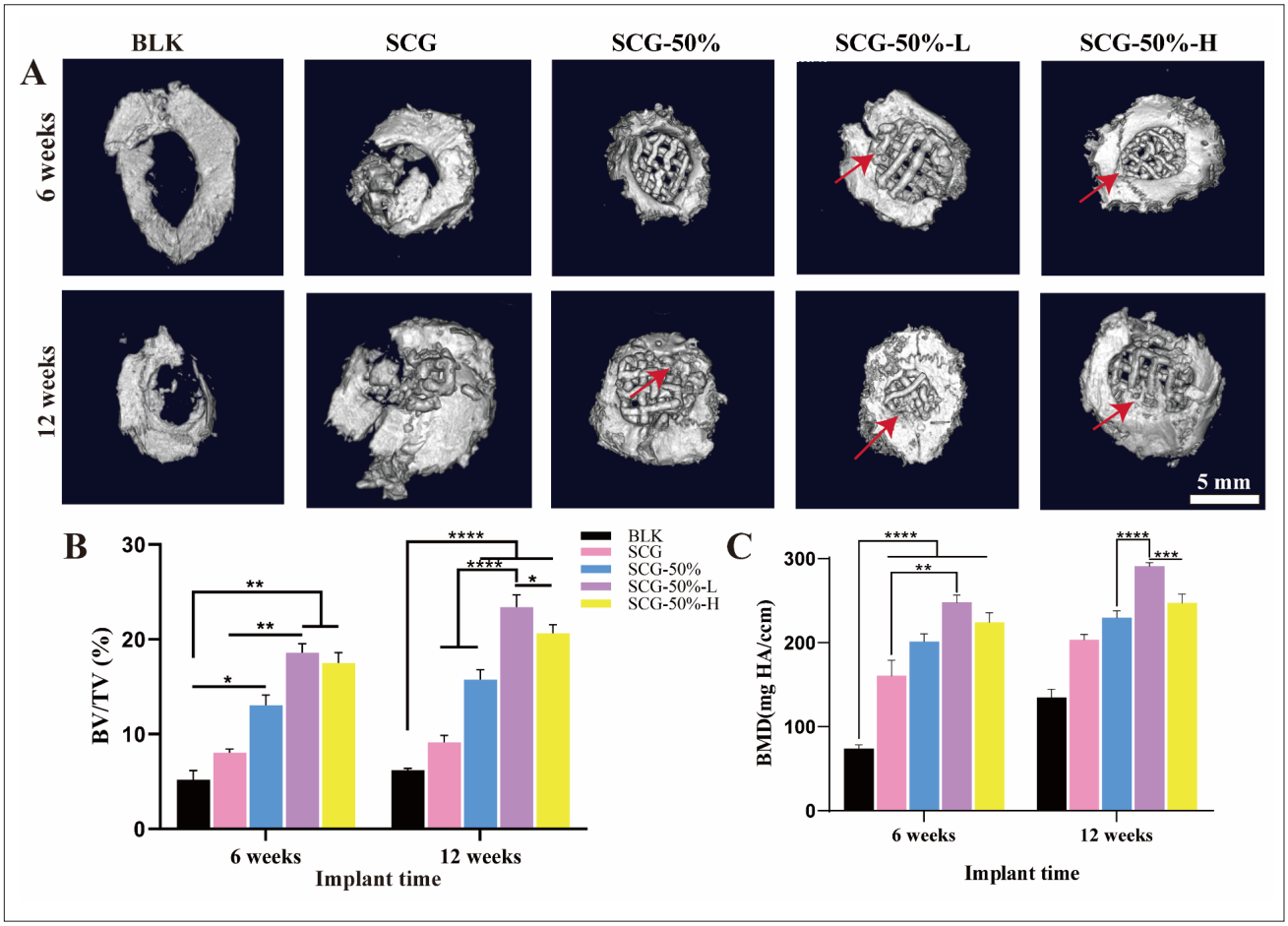

Figure 8. The *in vivo* development of large bone defects and the bone-healing effect. (A) Micro-computed tomography images of cranial defects in rats (red represents new bone tissue). Scale bar: 5 mm ; magnification: 2×. (B–C) Quantitative analysis of micro-computed tomography data: BV/TV (%) and BMD (mg HA/ccm). Statistical significance determined at $^{*}p < 0.05$, $^{**}p < 0.01$, $^{***}p < 0.001$, and $^{****}p < 0.0001$; $n=3$. Abbreviations: BLK, blank control; BMD, bone mineral density; BV/TV, bone volume/total volume; ns, not significant.

bone defect was primarily composed of loose collagen fibers. After 12 weeks of implantation, the control group exhibited minimal new bone formation, with the defect site predominantly filled with abundant muscle or fibrous tissue. The SCG and SCG-50% groups without drug loading showed a small amount of new bone at the interface with host bone tissue; however, the scaffold degraded and accumulated severely at the defect site, resulting in a lack of tissue ingrowth. In the drug-loaded groups, SCG-50%-L and SCG-50%-H, a substantial amount of new bone tissue was observed. These results collectively suggest that drug-loaded groups significantly promote bone regeneration. This finding is consistent with the H&E staining results.

Further analysis of this study indicates that the dual-crosslinked network scaffold significantly enhanced the mechanical properties and *in vivo* stability of the material. The incorporation of β-TCP not only provides additional mechanical support but also releases calcium ions and phosphate ions, promoting osteoblast adhesion and mineralization. EGCG may regulate anti-inflammatory signaling pathways such as nuclear factor kappa B, thereby creating a favorable immune microenvironment for bone regeneration. Compared with previous studies, our scaffold design achieved an optimized dual-network structure, whereas most earlier studies employed single-crosslinked systems and lacked biomimetic designs for the hierarchical porosity of cancellous bone, making it difficult to achieve effective bone regeneration through hydrogel networks. Although additional mechanistic experiments were not conducted in this study, existing literature sufficiently supports our explanations regarding the functions of dual-network hydrogels, β-TCP, and EGCG. Future work will further combine molecular-level experiments to provide a deeper understanding of these mechanisms and a more comprehensive understanding of the bone regeneration process.

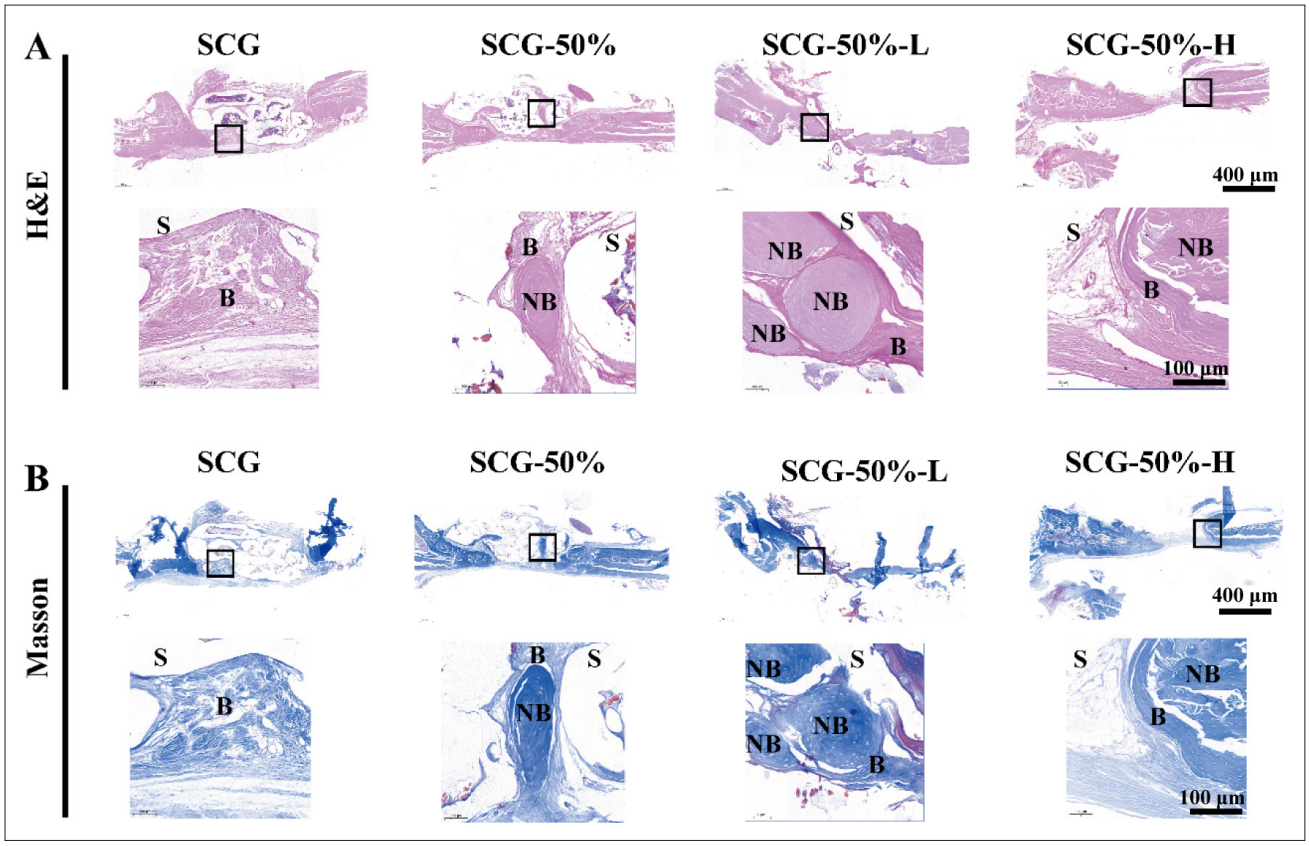

Figure 9. Histological analysis of calvaria 12 weeks after implantation. (A) Hematoxylin and eosin (H&E) staining results after 12 weeks of scaffold implantation, where B indicates host bone, NB indicates new bone, and S indicates scaffold. Scale bar: 400 μm; magnification: 4×. (B) Masson's trichrome (Masson) staining. Scale bar: 100 μm; magnification: 16×.

4. Conclusion

This study integrated the biomimetic tissue structure of hydrogels with the excellent bone-inducing capability and mechanical reinforcement ability of β-TCP. By combining these factors, a bioink was prepared. Through a pre-crosslinking strategy and regulation of printing parameters, personalized hydrogel-based composite scaffolds were 3D printed using extrusion-based bioprinting technology. By examining scaffold materials and relevant properties, we found that the scaffold exhibited excellent biomimetic structure, mechanical performance, drug-loading capacity, outstanding biocompatibility, and the ability to promote the expression of osteogenesis-related genes. *In vivo* experiments further demonstrated the scaffold's potent bone-inducing and bone-integrating capabilities. In summary, the artificially engineered bone scaffold developed in this study holds promise for clinical applications in addressing significant challenges related to bone loss.

Acknowledgments

None.

Funding

This study was supported by the National Science Foundation of China (NSFC, #82402822, 82202674), the Central Government of Sichuan through the Special Project of Local Science and Technology Development (#2024ZYD0155), the Health Commission of Sichuan Province Medical Science and Technology Program (#24QNMP036), and the Natural Science Foundation of Xiamen, China (3502Z20227124).

Conflict of interest

Xulin Hu serves as the Editorial Board Member of the journal, but did not in any way involve in the editorial and peer-review process conducted for this paper, directly or indirectly. Other authors declare they have no competing interests.

Author contributions

Conceptualization: Weizong Weng, Kainan Li
Formal analysis: Xulin Hu, Yixuan Lan, Wang Gong, Jiayu Liu
Investigation: Jian He, Weiming Zhao
Methodology: Zhen Zhang, Lijin Ning
Writing–original draft: Xulin Hu
Writing–review & editing: Shuhao Yang, Haoming Wu

Ethics approval and consent to participate

All animal experiments were conducted with the approval of the Ethics Committee of West China Hospital of Stomatology, Sichuan University (Approval number: WCHSIRB-D-2021-240).

Consent for publication

Not applicable

Availability of data

Data will be made available upon request to the corresponding author.

Reference

1. Wang Y, Zhang H, Hu Y, Jing Y, Geng Z, Su J. Bone repair biomaterials: a perspective from immunomodulation. *Adv Funct Mater.* 2022;32(51):2208639. doi: 10.1002/adfm.202208639
2. Batra P, Das S, Jain S. Correlation of radiovisuographic analysis of interdental and interradicular bone loss in furcation involvement of mandibular first molars: a retrospective study. *Indian J Dent Res*. 2018;29(3):329-332. doi: 10.4103/ijdr.IJDR_52_16. PMID: 29900917
3. Chang HY, Park SY, Kim JA, Kim YK, Lee HJ. Early radiographic diagnosis of peri-implantitis enhances the outcome of peri-implantitis treatment: a 5-year retrospective study after non-surgical treatment. *J Periodontal Implant Sci*. 2015;45(3):82-93. doi: 10.5051/jpis.2015.45.3.82
4. Kironde E, Sekimpi P, Kajja I, Mubiri P. Prevalence and patterns of traumatic bone loss following open long bone fractures at Mulago Hospital. *OTA Int*. 2019.2(1): e015-e015. doi: 10.1097/OI9.0000000000000015
5. Puisys A, Auzbikaviciute V, Minkauskaite A, et al. Early crestal bone loss: is it really loss? *Clin Case Rep*. 2019;7(10):1913-1915. doi: 10.1002/ccr3.2376
6. Zhou H, Liang B, Jiang H, Deng Z, Yu K. Magnesium-based biomaterials as emerging agents for bone repair and regeneration: from mechanism to application. *J Magnes Alloy*. 2021;9(3):779-804. doi: 10.1016/j.jma.2021.03.004
7. Du M, Chen J, Liu K, Xing H, Song C. Recent advances in biomedical engineering of nano-hydroxyapatite including dentistry, cancer treatment and bone repair. *Compos Part B Eng*. 2021;215:108790. doi: 10.1016/j.compositesb.2021.108790
8. Feng P, Zhao R Y, Tang W M, et al. Structural and functional adaptive artificial bone: materials, fabrications, and properties. *Adv Funct Mater*. 2023;33(23):2214726. doi: 10.1002/adfm.202214726
9. Nissen FI, Andreasen C, Borgen TT, Bjørnerem Å, Hansen AK. Cortical bone structure of the proximal femur and incident fractures. *Bone*. 2022;155:116284. doi: 10.1016/j.bone.2021.116284
10. Rodriguez-Palomo A, Ostergaard M, Birkedal H. Bone hierarchical structure: heterogeneity and uniformity. *Adv Funct Mater*. 2023;34(35):2307026. doi: 10.1002/adfm.202307026
11. Zhou C, Zhang XL, Ai J, et al. Chiral hierarchical structure of bone minerals. *Nano Res*. 2022;15(2):1295-1302. doi: 10.1007/s12274-021-3653-z
12. Yusof F, Sha'ban M, Azhim A. Decellularization strategies to engineer fibrocartilage bioscaffolds: a review. *J Biomater Tissue Eng*. 2021;11(8):1435-1451. doi: 10.1166/jbt.2021.2740
13. He J, Fang J, Wei P, *et al.* Cancellous bone-like porous Fe@Zn scaffolds with core-shell-structured skeletons for biodegradable bone implants. *Acta Biomater*. 2021;121:665-681. doi: 10.1016/j.actbio.2020.11.032
14. Yoon SJ, Kim SH, Choi JW, Chun HJ, Yang DH. Guided cortical and cancellous bone formation using a minimally invasive technique of BMSC- and BMP-2-laden visible light-cured carboxymethyl chitosan hydrogels. *Int J Biol Macromol*. 2023;227:641-653. doi: 10.1016/j.ijbiomac.2022.12.13
15. Zhao ZY, Li G, Ruan HT, et al. Capturing magnesium ions via microfluidic hydrogel microspheres for promoting cancellous bone regeneration. *ACS Nano*. 2021;15(8):13041-130540. doi: 10.1021/acsnano.1c02147
16. Hu X, Lin Z, He J, et al. Recent progress in 3D printing degradable polylactic acid-based bone repair scaffold for the application of cancellous bone defect. *MedComm Biomater Appl*. 2022;1(1):e14. doi: 10.1002/mba2.14
17. Riggs C, Goodship A. Bone structure and function. *Fractures in the Horse*. 2022:11-27. doi: 10.1002/9781119431749.ch2

18. Li C, Du YW, Zhang TT, et al. "Genetic scissors" CRISPR/Cas9 genome editing cutting-edge biocarrier technology for bone and cartilage repair. *Bioact Mater*. 2023;22:254-273. doi: 10.1016/j.bioactmat.2022.09.026

19. Salhotra A, Shah HN, Levi B, Longaker MT. Mechanisms of bone development and repair. *Nat Rev Mol Cell Biol*. 2020;21(11):696-711. doi: 10.1038/s41580-020-00279-w

20. Seidi A, Ramalingam M. Engineering of gradient biomaterials as biomimetic systems for tissue engineering. *J Biomater Tissue Eng*. 2011;1(2):139-148. doi: 10.1166/jbt.2011.1020

21. Li J, Chen Q, Zhang Q, et al. Improving mechanical properties and biocompatibilities by highly oriented long chain branching poly(lactic acid) with bionic surface structures. *ACS Appl Mater Interfaces*. 2020;12(12):14365-14375. doi: 10.1021/acsami.9b20264

22. Qi T, Zhang X, Gu X, Cui S. Experimental study on repairing peripheral nerve defects with novel bionic tissue engineering. *Adv Healthc Mater*. 2023;12(17):e2203199. doi: 10.1002/adhm.202203199

23. Wang Y, Jiang X, Li X, et al. Bionic ordered structured hydrogels: structure types, design strategies, optimization mechanism of mechanical properties and applications. *Mater Horiz*. 2023;10(10):4033-4058. doi: 10.1039/d3mh00326d

24. Wang L, Li AF, Zhang D, et al. Injectable double-network hydrogel for corneal repair. *Chem Eng J*. 2023;455:140698. doi: 10.1016/j.cej.2022.140698.

25. Zhu WX, Zhou Z, Huang YT, et al. A versatile 3D-printable hydrogel for antichondrosarcoma, antibacterial, and tissue repair. *J Mater Sci Technol*. 2023;136:200-211. doi: 10.1016/j.jmst.2022.07.010

26. Ahmed EM. Hydrogel: preparation, characterization, and applications: a review. *J Adv Res*. 2015;6(2):105-121. doi: 10.1016/j.jare.2013.07.006

27. Lee KY, Mooney DJ. Alginate: properties and biomedical applications. *Prog Polym Sci*. 2012;37(1):106-126. doi: 10.1016/j.progpolymsci.2011.06.003

28. Liang YP, He JH, Guo BL. Functional hydrogels as wound dressing to enhance wound healing. *ACS Nano*. 2021;15(8):12687-12722. doi: 10.1021/acsnano.1c04206

29. Correa CS, Grosskopf AK, Hernandez HL, Chan D, Appel EA. Translational applications of hydrogels. *Chem Rev*. 2021;121(18):11385-11457. doi: 10.1021/acs.chemrev.0c01177

30. Nie R, Sun Y, Lv H, et al. 3D printing of MXene composite hydrogel scaffolds for photothermal antibacterial activity and bone regeneration in infected bone defect models. *Nanoscale*. 2022;14(22):8112-8129. doi: 10.1039/D2NR02176E

31. Gong JP, Katsuyama Y, Kurokawa T, Osada Y. Double-network hydrogels with extremely high mechanical strength. *Adv Mater*. 2003;15(14):1155-1158. doi: 10.1002/adma.200304907

32. Aldana AA, Houben S, Moroni L, Baker MB, Pitet LM. Trends in double networks as bioprintable and injectable hydrogel scaffolds for tissue regeneration. *ACS Biomater Sci Eng*. 2021;7(9):4077-4101. doi: 10.1021/acsbiomaterials.0c01749

33. Xu X, Jerca VV, Hoogenboom R. Bioinspired double network hydrogels: from covalent double network hydrogels via hybrid double network hydrogels to physical double network hydrogels. *Mater Horiz*. 2021;8(4):1173-1188. doi: 10.1039/d0mh01514h

34. Yang J, Li K, Tang C, et al. Recent progress in double network elastomers: one plus one is greater than two. *Adv Funct Mater*. 2022;32(19):2110244. doi: 10.1002/adfm.202110244

35. Gao N, Zhang Y, Yang Z, et al. Ba2+/Ca2+ co-crosslinked alginate hydrogel filtration membrane with high strength, high flux and stability for dye/salt separation. *Chin Chem Lett*. 2023;35(5):108820. doi: 10.1016/j.cclet.2023.108820

36. Zhang A, Wang F, Chen L, et al. 3D printing hydrogels for actuators: a review. *Chin Chem Lett*. 2021;32(10):2923-2932. doi: 10.1016/j.cclet.2021.03.073

37. Wang Y, Jiao Y, Zeng Z, Chang J, Yang C, Dong Z. Three-dimensional printed Zn2SiO4/sodium alginate composite scaffold with multiple biological functions for tendon-to-bone repair. *MedComm Biomater Appl*. 2023;2(4):e61. doi: 10.1002/mba2.61

38. Kankariya Y, Chatterjee B. Biomedical application of chitosan and chitosan derivatives: a comprehensive review. *Curr Pharm Des*. 2023;29(17):1311-1325. doi: 10.2174/1381612829666230524153002

39. Manna S, Seth A, Gupta P, et al. Chitosan derivatives as carriers for drug delivery and biomedical applications. ACS *Biomater Sci Eng*. 2023;9(5):2181-2202. doi: 10.1007/978-981-15-0263-7

40. Sacco P, Pedroso-Santana S, Kumar Y, Joly N, Martin P, Bocchetta P. Ionotropic gelation of chitosan flat structures and potential applications. *Molecules*. 2021;26(3):660. doi: 10.3390/molecules26030660

41. Yan D, Li Y, Liu Y, Li N, Zhang X, Yan C. Antimicrobial properties of chitosan and chitosan derivatives in the treatment of enteric infections. *Molecules*. 2021;26(23):7136. doi: 10.3390/molecules26237136

42. Xulin H, Hu L, Liang Q, et al. 369Fabrication of 3D gel-printed β-tricalcium phosphate/titanium dioxide porous

scaffolds for cancellous bone tissue engineering. *Int J Bioprint*. 2023;9(2):673. Published 2023 Jan 19. doi: 10.18063/ijb.v9i2.673

43. Peres I, Rocha S, do Carmo Pereira M, Coelho M, Rangel M, Ivanova G. NMR structural analysis of epigallocatechin gallate loaded polysaccharide nanoparticles. *Carbohydr Polym*. 2010;82(3):861-866. doi: 10.1016/j.carbpol.2010.06.007

44. Zhang S, Mao B, Cui S, et al. Absorption, metabolism, bioactivity, and biotransformation of epigallocatechin gallate. *Crit Rev Food Sci Nutr.* 2024;64(19):6546-6566. doi: 10.1080/10408398.2023.2170972

45. Guo Z, Liu W, Liu T, et al. Engineered exosome hybrid copper nanoscale antibiotics facilitate simultaneous self-assembly imaging and elimination of intracellular multidrug-resistant superbugs. *Chin Chem Lett.* 2023;35(7):109060. doi: 10.1016/j.cclet.2023.109060

46. Baranwal A, Aggarwal P, Rai A, Kumar N. Pharmacological actions and underlying mechanisms of catechin: a review. *Mini Rev Med Chem.* 2022;22(5):821-833. doi: 10.2174/1389557521666210902162120

47. Cabezas Perez RJ, Ávila Rodríguez MF, Rosero Salazar DH. Exogenous antioxidants in remyelination and skeletal muscle recovery. *Biomedicines.* 2022;10(10):2557. doi: 10.3390/biomedicines10102557

48. Spicer PP, Kretlow JD, Young S, Jansen JA, Kasper FK, Mikos AG. Evaluation of bone regeneration using the rat critical size calvarial defect. *Nat Protoc.* 2012;7(10):1918-1929. doi: 10.1038/nprot.2012.113